Research Square

Preprints are preliminary reports that have not undergone peer review.
They should not be considered conclusive, used to inform clinical practice,
or referenced by the media as validated information.

Human forebrain assembloids modeling a neurodevelopmental disorder reveals neural circuit deficits via DNA damage

Karun Singh

Karun.Singh@uhn.ca

University Health Network

Savannah Kilpatrick

University Health Network

Lingdi Nie

Donald K Johnson Eye Institute, University Health Network

Xavier Rutherford

University of Toronto

Zahra Dargaei

University Health Network

Jarryll Uy

University Health Network

Anran Cheng

University Health Network

Yi Pan

University Health Network

He Tian Chen

University Health Network

Jennifer Howe

The Hospital for Sick Children

Nizar Chetoui

CERVO Brain Research Center

Marie-Eve Paquet

CERVO Brain Research Center

Kristin Hope

University Health Network

Stephen Scherer

The Hospital for Sick Children

Jaideep Bains

University Health Network

Article

Keywords:

Posted Date: November 14th, 2025

DOI: https://doi.org/10.21203/rs.3.rs-7957934/v1

License: This work is licensed under a Creative Commons Attribution 4.0 International License.
Read Full License

Additional Declarations: Yes there is potential Competing Interest. Savannah Kilpatrick is employed by Genentech. Other authors declare no conflict of interest.

Human forebrain assembloids modeling a neurodevelopmental disorder reveals neural circuit deficits via DNA damage

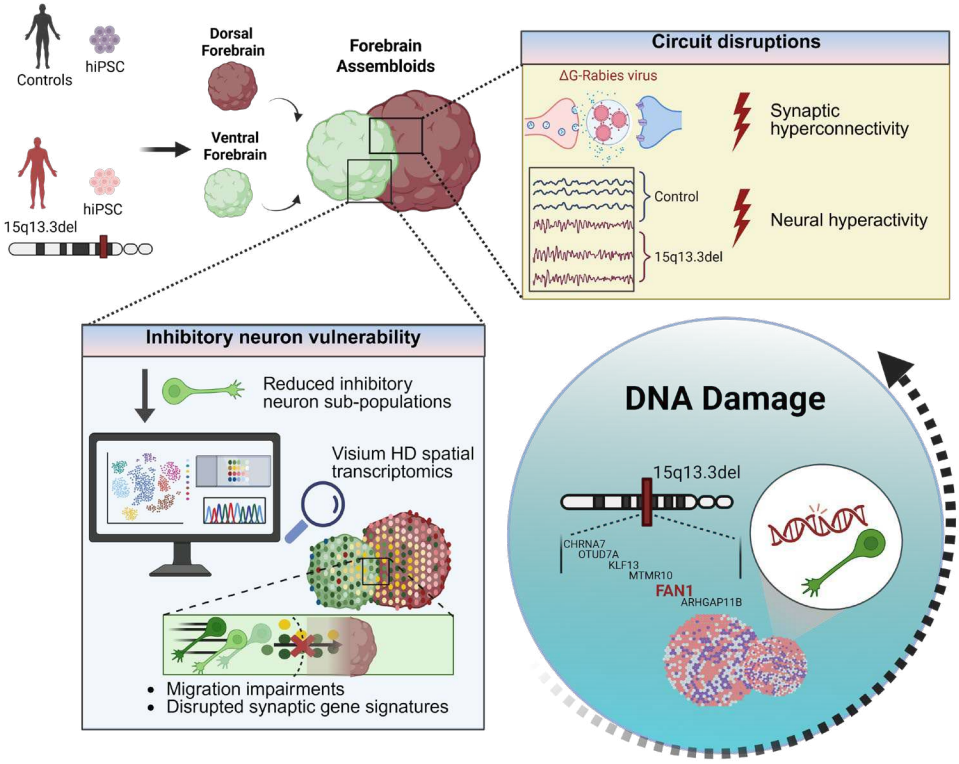
Savannah Kilpatrick[1*], Lingdi Nie[1*], Xavier E. Rutherford[2], Zahra Dargaei[1], Jarryll A. Uy[1,2], Anran A. Cheng[1], Yi Pan[1], He Tian Chen[4,5], Jennifer L. Howe[6], Nizar Chetoui[7], Marie-Eve Paquet[7], Kristin J. Hope[5], Stephen W. Scherer[6], Jaideep S. Bains[1], Karun K. Singh[1,2,3,].**

[1] Donald K Johnson Eye Institute and Krembil Research Institute, University Health Network, Toronto, ON, Canada.
[2] Department of Laboratory Medicine and Pathobiology, Faculty of Medicine, University of Toronto, Toronto, ON, Canada.
[3] Department of Ophthalmology & Vision Sciences, Faculty of Medicine, University of Toronto, Toronto, ON, Canada.
[4] Princess Margaret Cancer Research Institute, University Health Network, Toronto, ON, Canada.
[5] Department of Medical Biophysics, University of Toronto, Toronto, ON, Canada
[6] The Centre for Applied Genomics, The Hospital for Sick Children, Toronto, ON M5G 0A4, Canada
[7] CERVO Brain Research Center, University of Laval, Quebec City, PQ G1J 2G3, Canada

*Equal contributions

**Correspondence: Karun K. Singh; karun.singh@uhn.ca

Cortical circuit dysfunction is strongly linked to neurodevelopmental disorders (NDDs). The mechanisms by which disruptions in early cortical development lead to defects in mature human neural circuit function are not well understood. Here, using human forebrain assembloids from individuals with the 15q13.3 microdeletion syndrome, we identified dysregulation of early gene networks in cortical neurons that results in migration deficits, reduced synaptic connections and decreased activity in inhibitory neuron subpopulations. These early inhibitory defects resulted in hyperactive networks and synaptic hyperconnectivity in maturing forebrain assembloids. Using unbiased spatial transcriptomics, we revealed regional transcriptional and cell-cell signaling disturbances, including elevated DNA damage in inhibitory neurons linked to Fanconi anemia-associated nuclease 1 (FAN1), a DNA repair enzyme. Collectively, our findings establish a human brain assembloid framework that reveals how early DNA damage–related mechanisms and cell type–specific vulnerabilities contribute to neural circuit dysfunction, providing mechanistic insight into the neurodevelopmental and neuropsychiatric features of the 15q13.3 microdeletion.



Main

Disruptions to cortical development and neural circuit function are a major contributor to cognitive dysfunction and clinical phenotypes observed in epilepsy, autism spectrum disorder (ASD), and other neurodevelopmental disorders (NDDs). Progress has been made to understand how abnormal postnatal development and function of neural circuits lead to NDDs; however, this later-stage screening leaves a considerable gap in understanding how they arise, given that many NDD-associated genes are also expressed during prenatal brain development. Specifically, our understanding of how early (fetal) brain developmental deficits are linked to mature circuit dysfunction, particularly in the human brain, remains poorly studied. Human pluripotent stem cell-derived organoids have emerged as powerful models to fill this gap in knowledge by understanding the early stages of circuit dysfunction in the human brain[1–8]. Further, the fusion of organoids into neural assembloids offers opportunities to study 3D human neuronal connectivity at the cell-type level[2,9–15]. Individual brain cell types have been explored in isolation in neural assembloids[2,16–19]; however, the developmental molecular changes in local cellular networks and the microenvironment that leads to human neural circuit dysfunction are not well understood.

One of the major genetic risk factors that contribute to a range of neurodevelopmental and neuropsychiatric disorders are copy number variations (CNVs)[20–24]. The 15q13.3 microdeletion is a recurrent CNV that leads to a range of clinical manifestations including intellectual disability, seizures, schizophrenia, and ASD[25–29]. Previous efforts have identified postnatal excitatory neuron deficits in the 15q13.3 deletion mouse or two-dimensional patient iPSC-neuronal models[30–33]. Human organoids modeling other genetic NDDs also reveal abnormal excitatory neurogenesis and neuron development[3,7,34–38]. The participation of other cell types to NDD pathology remains understudied in a human context and largely precludes our understanding of how the highly diverse inhibitory (GABAergic) neuron subpopulations contribute to neural circuit dysfunction. Single cell genomics of the typically developing human brain has revealed new insight into inhibitory neuron development and diversity,[39–43] but insight from human NDD-associated brain tissue remains understudied. The preservation of human inhibitory neuron diversity in organoids and assembloids offers a unique opportunity

to obtain new insights into developmental GABAergic neuronal lineages defects that lead to subsequent cortical neural circuit dysfunction[2,12,14,44–48]. Further, the emergence of spatial transcriptomic technologies allows an understanding of the organizational and molecular basis of cell type-specific mechanisms, to elucidate the early stages of disease pathogenesis.

To investigate developmental cell type-specific and microenvironment-relevant alterations in NDDs, we generated human neural forebrain organoids and assembloids from individuals with the 15q13.3 microdeletion syndrome (15q13.3del). Multi-omic screening across forebrain organoid and assembloid models revealed distinct transcriptional dysregulation in both excitatory and inhibitory neuron lineages. Further investigation of inhibitory subpopulations revealed alterations to maturation, with neurons of the medial ganglionic eminence (MGE) displaying synaptic and functional deficits that lead to network hyperactivity and monosynaptic connectivity in cortical organoid tissue. Finally, we established a spatial biology pipeline at single cell resolution and revealed unique microenvironment and cell type-specific signaling alterations to distinct neuronal lineages within assembloids. This included FAN1-related DNA damage enrichment in developing inhibitory neurons. Collectively, our results reveal that early cell type-specific DNA damage defects in local microcircuits can lead to functional alterations in human brain assembloid models, which may contribute to the presentations of epilepsy and neuropsychiatric disorders in individuals with the 15q13.3 microdeletion syndrome.

Results

Single cell and bulk RNA sequencing of forebrain organoid models reveals deficits amongst excitatory and inhibitory neural lineages

To examine the impact of the 15q13.3 microdeletion (15q13.3del) on various neural cell types during early (prenatal) neurodevelopment, we leveraged guided dorsal and ventral forebrain organoids. These model systems replicate cortical excitatory and inhibitory neurons, respectively, as they enrich for these cell types with high fidelity and reduced variability compared to unguided neural organoid protocols[49]. Our cohort of control (familial) and 15q13.3del patient iPSC lines has been previously reported[30], with the addition of new independent and unrelated lines (4 familial control lines and 5 15q13.3del patient iPSC lines in total, Table 1) that were positive for pluripotency markers (Extended Data Fig. 1a), displayed a normal karyotype (Extended Data Fig. 1b) and similar breakpoint on the chromosome 15q13.3 BP4-5 region (Extended Data Fig. 1c,d).

To quantify transcriptional changes in the 15q13.3del background, bulk RNA sequencing (bulk RNA Seq) was conducted at day 50 and 100 of differentiation using dorsal and ventral organoid tissue from the entire cohort (Fig. 1a,b and Extended Data Fig. 2). Both timepoints produced heterozygous expression of the 15q13.3 genes in patient-derived organoids (Extended Data Fig. 2c), and initial differential gene expression analysis yielded 1,534, 3,694, 3,033, and 5,169 differentially expressed genes (DEGs) within day 50 dorsal, day 100 dorsal, day 50 ventral, and day 100 ventral tissue, respectively (Wald test, FDR < 0.05, Supplementary Table 1). These genes were only partially shared with our previous bulk RNA Seq mouse study in 15q13.3del mice[31], likely due to differences in developmental stage of the mouse brain versus organoid tissue. Interestingly, amongst the genes at the 15q13.3 locus, those most highly expressed included KLF13 and FAN1, whereas OTUD7A and CHRNA7, which we and others have proposed as drivers of the 15q13.3del syndrome due to their expression in the postnatal brain[30–32,50–55], were weakly expressed in both the bulk and single cell RNA sequencing (scRNA Seq) datasets (Extended Data Fig. 2d and Extended Data Fig. 3d,e). The elevated expression of FAN1 and KLF13 was corroborated with extracted single cell gene expression data from the developing human fetal brain (Extended Data Fig. 3i). This suggests that at prenatal time points, pathways independent of CHRNA7 and OTUD7A may drive the development of the syndrome. In forebrain organoids, all 15q13.3 genes were significantly reduced in 15q13.3del patient dorsal and ventral tissue, confirming heterozygosity in organoids (Extended Data Fig. 2c and Extended Data Fig. 3e).

We next sought to identify signaling pathways associated with the 15q13.3del. For this, we performed gene ontology (GO) analysis on the DEGs from the bulk-seq data from dorsal and ventral organoids. We found different pathways were enriched between dorsal and ventral tissue and across the day 50 and 100 time points. Interestingly, we

found an enrichment of synapse organization and glutamate receptor binding pathways in mature dorsal and immature ventral forebrain organoids, respectively (Fig. 1b, FDR < 0.05), suggesting that neural dysfunction occurs throughout their development. Further, we identified potential pathways related to DNA damage and repair, and DNA binding in dorsal and ventral lineages, respectively, which may be linked to the transcriptional alterations (Fig. 1b).

To identify cell types contributing to the changes in gene expression, we performed scRNA Seq on dorsal and ventral forebrain organoids from control and 15q13.3del patients at day 100 when there is a diversity of cell types[9]. Amongst the 159, 084 cells that passed our quality control process (see **Methods,** Extended Data Fig. 3c), we identified radial glial cell types, intermediate progenitors, excitatory neurons, and inhibitory neurons expressing markers of the caudal and medial ganglionic eminences (CGE/MGE) (Fig. 1c). Consistent with previous reports, the MGE-like inhibitory neuron populations originated from the ventral tissue, whereas the CGE-like inhibitory neurons were dorsal-derived[56] (Extended Data Fig. 3a,b). We used differential gene expression (Supplementary Table 2) analysis to identify which cell types were most affected transcriptionally by the 15q13.3del. We applied a stringent filter (see **Methods**) to extract highly dysregulated genes and identified mature excitatory and inhibitory neural lineages as the highest contributors towards gene dysregulation (Fig. 1d).

We next ordered the dorsal- and ventral-derived cells along a pseudotime axis to infer how the trajectory of each cell type was altered across development[57]. Pseudo-temporal modeling ordered the cells from proliferative radial glia to post-mitotic neurons of various lineages (Extended Data Fig. 3h), in line with early cortical development and neural organoid models[58,59]. We observed a significant alteration in the pseudotime density distribution in the collective dataset between genotypes (Fig. 1e), indicating an abnormal developmental trajectory of 15q13.3del neural organoids[57]. These findings suggest that deficits exist in both inhibitory and excitatory neurons amongst multiple neural organoid model systems, but that they may be subtype specific.

Upon examination of the MGE- and CGE-inhibitory neurons, we observed opposite trends in the directionality of gene dysregulation; with the MGE inhibitory neurons producing mainly downregulated genes (Fig. 1f, 66.60%,) whereas the majority (>85%) of the CGE-inhibitory DEGs were upregulated (Fig. 1g), suggesting inhibitory neurons are vulnerable through different mechanisms in the 15q13.3 microdeletion. In contrast, the mature excitatory neuron population produced roughly equal numbers of up- and down-regulated genes (Fig. 1h). Despite the differences in gene regulation, synaptic gene ontology analysis (SynGO)[60] of the mature excitatory neuron and the MGE- and CGE-inhibitory neuron gene sets confirmed that the DEGs in all cell types were enriched at the synapse (Fig. 1i-k), with the MGE-inhibitory neurons possessing the highest percentage of pre- (9.8% of DEGs) and postsynaptic (12.23% of DEGs) genes, including NRXN1, NCAM1, NCAM1, PSD2 SYNGAP1, and GABBR1 (-log10 Qvalue >10).

Both excitatory and inhibitory neural lineages showed alterations to pseudotime trajectory and enrichment of synaptic gene modules pertaining to neural activity (Fig. 1l-n). MGE-derived inhibitory neurons showed significant reductions in synaptic gene module expression (Fig. 1l, Wilcoxon $p<0.001$), whereas CGE-derived inhibitory neurons and mature excitatory neurons displayed significant increases (Fig. 1m-n, Wilcoxon $p <0.001$). Together, these results indicate distinct, lineage-specific disruptions to synaptic gene networks across excitatory and inhibitory populations in 15q13.3 microdeletion organoid models.

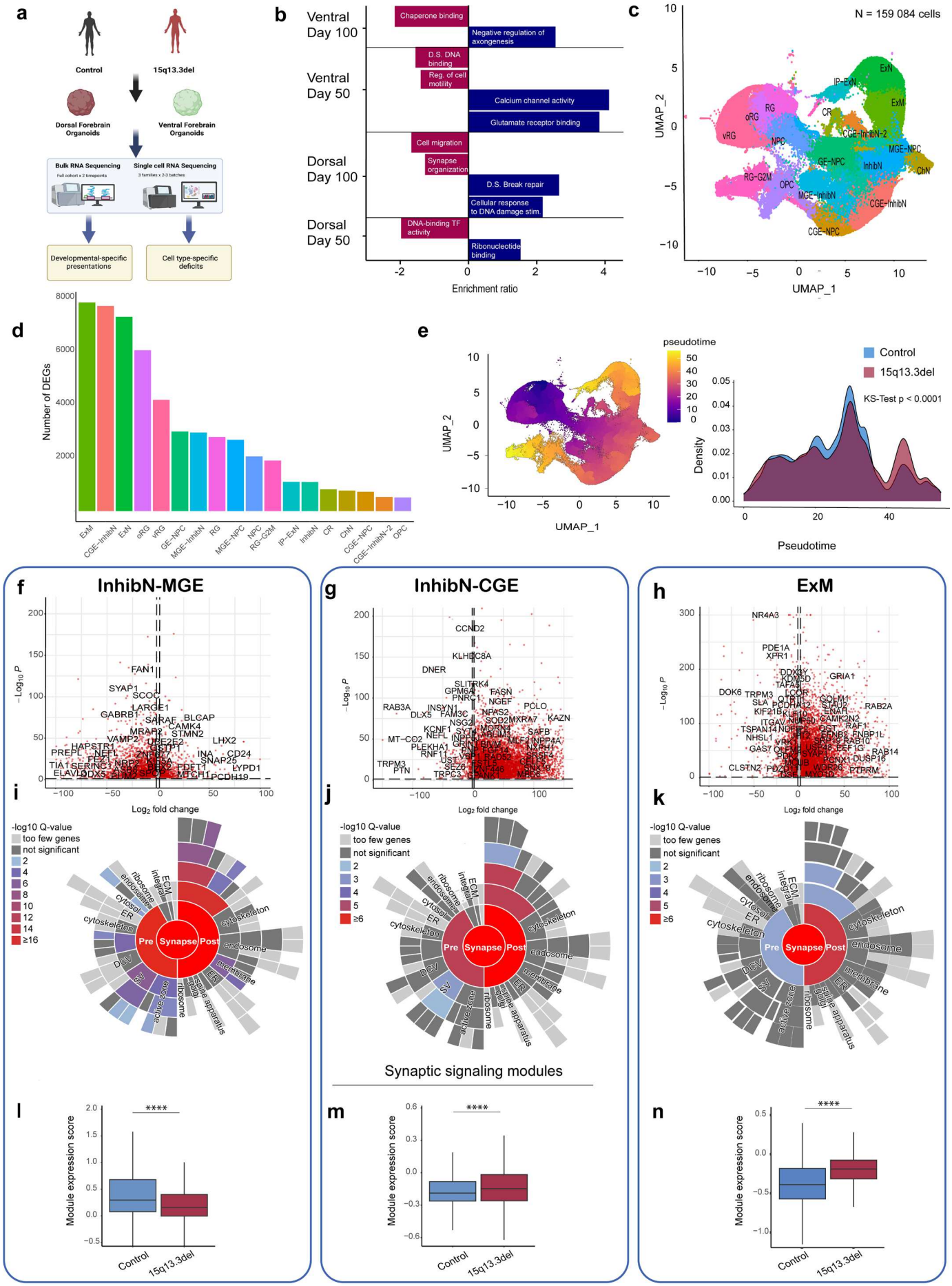


Fig. 1: Multi-transcriptomics characterization of inhibitory neuron sub-type vulnerabilities in guided

15q13.3del neural organoids.

a, Schematic of bioinformatic and functional approaches to study 15q13.3 microdeletion syndrome (15q13.3del) patients. **b,** Select downregulated (red) and upregulated (blue) terms from Gene ontology (GO) enrichment analysis of day 50 and day 100 dorsal and ventral forebrain bulk RNA sequencing (N = 5 15q13.3del patients and familial controls, pAdj < 0.05). **c,** Uniform Manifold Approximation and Projection (UMAP) plot of day 100 dorsal and ventral forebrain scRNA Seq (N = 2-3 batches of three 15q13.3del families, n = 159 084 cells). **d,** Number of highly differentially expressed genes (DEGs, Wilcoxon pAdj < 1e-4, log2(0.8)< Log2FC > log2(1.2)) per cell type. **e,** Pseudotime partition UMAP plot (top) and density plot (bottom) of aggregate dataset stratified by genotype (Kolmogorov-Smirnov test p = 2.2e-16). **f-h,** Volcano plots with select genes highlighted and **j-k,** SynGO synaptic enrichment sunburst plots of highly differentially expressed genes derived from MGE-InhibNs, CGE-InhibNs, and ExM neuron clusters. The color of the box shows the ratio for enrichment (q-value < 0.05). **l-n,** Pseudotime synaptic gene module expression in MGE-InhibNs (Wilcoxon pAdj = 6.78198e-81), InhibN-CGE (pAdj = 1.024264e-29), and ExM neurons (pAdj = 6.119136e-245). Cell annotations: (ChN) *cholinergic neurons*, (CR cells) *Cajal-Retzius cells*, (GE NPC) *ganglionic eminence NPC*, (ExN) *Excitatory neurons*, (ExM) *mature excitatory neurons*, (NPC-ExN) *neural progenitor cell-excitatory neurons*, (NPC-/InhibN-CGE/MGE) *neural progenitor-inhibitory neuron caudal ganglionic eminence/medial ganglionic eminence*, (OPC) *oligodendrocyte progenitor cell*, (oRG) *outer radial glia*, (RG) *radial glia*, (RG-G2M) *cycling radial glia,* (Unk) *unknown*, (vRG) *ventral radial glia*.

Multi-scale circuit interrogation of inhibitory neurons reveals migration and synaptic deficits in 15q13.3del forebrain assembloids.

Our multi-transcriptomic data suggest that unique and convergent pathways disrupt different neural subtypes in the human 15q13.3del background. We have previously characterized deficits in 15q13.3del patient-derived 2D NGN2-excitatory neural cultures[30]; however, this protocol does not capture neural stem cell transitions nor cell types outside of the excitatory neural lineage. To better profile inhibitory neural lineages, we utilized canonical MGE subtype markers NKX2-1 and SST to identify reductions to MGE-like inhibitory neurons in ventral organoid tissue (Fig. 2a).

The loss of inhibitory neuron subtypes warranted further exploration on a circuit level. By fusing the dorsal and ventral forebrain tissue, we leveraged an established assembloid model system for its ability to mimic early aspects of neural circuit formation, and importantly, provide the microenvironment necessary for ventrally-derived inhibitory neuron migration[10] into the dorsal microenvironment[2, 9, 14], simulating the tangential migration of fetal interneurons in the developing cortex[9]. To sparsely label neurons and progenitors in each organoid, we infected 15q13.3del hiPSCs with lentiviruses harboring hSYN-rTTA and either pTET-CMV-eGFP (ventral) or pTET-CMV-mCherry (dorsal) (Extended Data Fig. 4a,b)[62]. We fused the organoids once the patterning media components were shared between lineages (day 25) to increase the duration of excitatory-inhibitory neural co-culture. We also created different genotypes and lineage fusions to generate four distinct forebrain assembloid combinations to measure cell-autonomous and non-cell-autonomous effects (Fig. 2b). After confirming that the MGE lineage was retained post-migration (Extended Data Fig. 4c), we quantified interneuron migration after one month of assembloid formation[16]. Specifically, we quantified the proportion of hSYN-rTTA/pTET-CMV-eGFP$^+$ ventral inhibitory neurons that migrated into the dorsal microenvironment using tissue clearing and light sheet microscopy (see **Methods**). We discovered two assembloid combinations to have impaired migration (Fig. 2c): the CTRL-DEL combination (control dorsal combined with 15q13,3del ventral organoid, ~2.6 fold-reduction, p <0.001) as well as the DEL-DEL combination (~4.9 fold-reduction reduction, p< 0.0001), suggesting cell-autonomous mechanisms. Given that interneuron maturation and subtype specification is influenced by their positioning in the developing cortex[39,63], exposure to environmental cues[64,65], and the excitability of neighboring cells[66–68], we also examined neurite morphology of the migrating ventral inhibitory neurons. We found reductions to the primary neurite length in all but the CTRL-CTRL combination (Fig. 2d), suggesting both cell-autonomous and non-cell-autonomous mechanisms.

To examine potential correlations to human inhibitory neuron synaptic dysfunction, we used monosynaptic rabies tracing[69] using an AAV-TVA helper virus under the DLX5/6 promoter (AAV-hDlx-TVA-mCherry-2A-oG) to label human inhibitory neuron-specific synapses (Fig. 2e). We infected 5-month forebrain assembloids using RABV-EnvA-deltaG-GFP-F2 and optically cleared the tissue for light sheet microscopy to achieve an unbiased spatial assessment of the synaptic connectome. Control experiments revealed that in the absence of TVA expression, RABV-ENVA-ΔG-

GFP does not infect the organoids, demonstrating the specificity of the system (Extended Data Fig. 4d). We quantified the connectivity ratio as the proportion of presynaptic/postsynaptic neurons and found a total decrease throughout the assembloid tissue (Fig. 2f)[70], suggesting that 15q13.3del inhibitory neurons receive less synaptic input. Collectively, we identifed developmental and synaptic deficits in human 15q13.3del inhibitory, indicating dysfunction of this cell type may drive functional defects associated with this NDD.

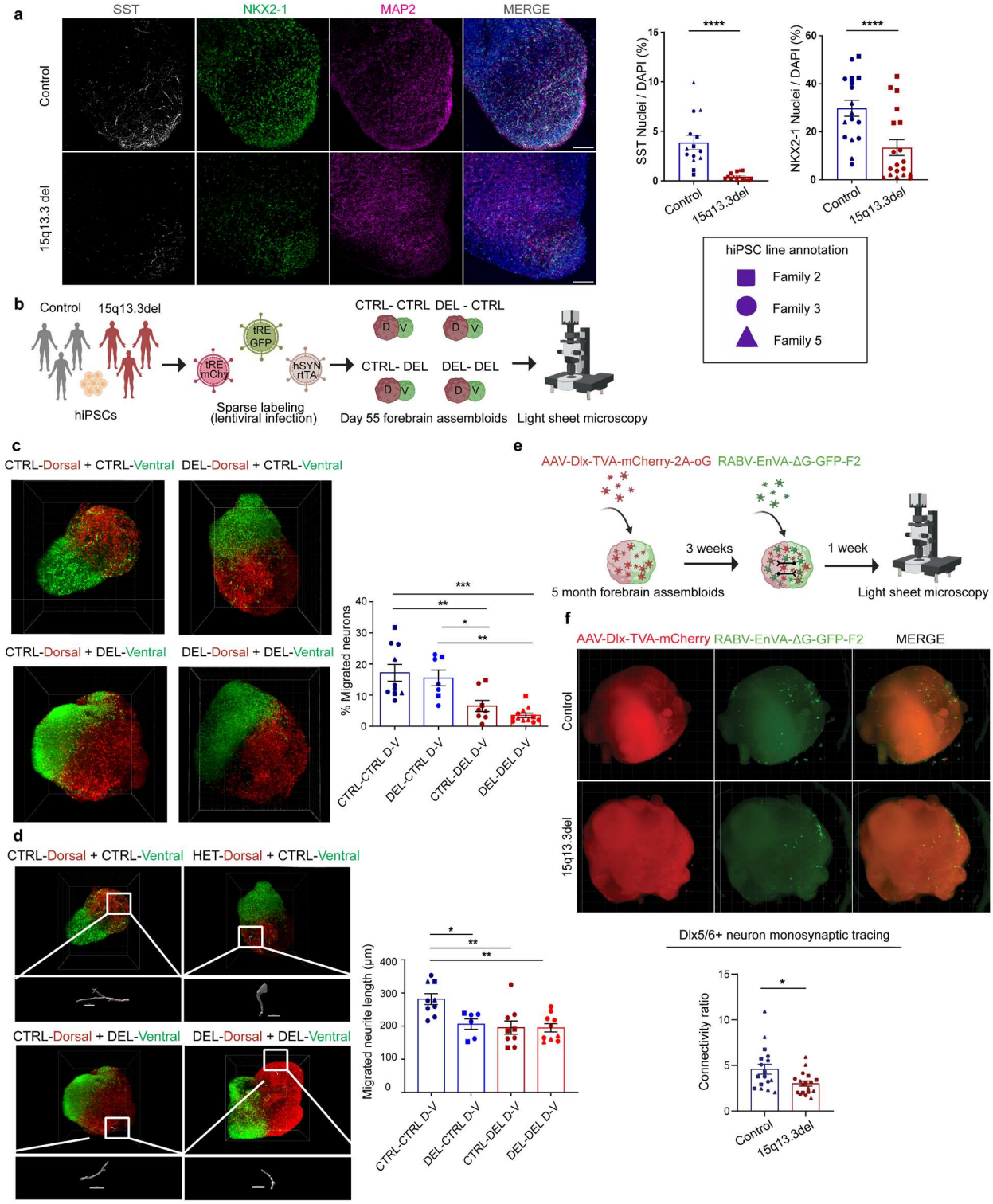


Fig. 2: Functional profiling of 15q13.3del assembloids captures deficits in inhibitory neuron motility and integration of synaptic connectome.

a, Quantification of SST+ and NKX2-1+ inhibitory neurons in day 50 15q13.3del ventral forebrain organoids. **Left**: representative 20x images, **right**: quantification of N = 3 families, control n = 17 and 15q13.3del n = 19 organoids. Scale bars represent 100 µm. **b,** Viral

labeling strategy for inhibitory neuron migration assays. **c,** Representative 4x reconstructed 3D images of all combinations for migration experiment with proportion of migrated cells (N = 3 families, n = 7-9 assembloids/combination). **d,** IMARIS reconstruction of a migrating neuron with average neurite length per assembloid. Scale bars represent 100 μm (N = 3 families, n = 7-12 assembloids per combination). **e,** Rabies viral labeling strategy for profiling inhibitory neuron-specific synaptic connections in 15q13.3del assembloids. **f,** Representative 4x IMARIS images of 5-month assembloid infected with AAV-Dlx5/6-TVA-mCherry and RABV-EnvA-deltaG-GFP-F2 and quantified connectivity ratio of synaptically connected neurons (N = 3 families, n = 21 assembloids per genotype). Error bars represent mean ± SEM; *p<0.05, **p<0.01, ***p<0.001, ****p<0.0001.

Spatial transcriptomics at single cell resolution identifies cellular communication and microenvironment deficits to inhibitory neuron subpopulations in 15q13.3del forebrain assembloids.

Our multi-transcriptomic and functional phenotyping indicates that human inhibitory neuron dysfunction is evident at the population and circuit level in 15q13.3del patient organoids and assembloids. To investigate the underlying mechanism within the assembloid, we optimized the 10x Genomics Visium HD platform for spatial transcriptomics across three independent 15q13.3del assembloid lines (Fig. 3a). This high-resolution platform (4 μm) enables single-cell–level label transfer using our forebrain scRNA-seq dataset as a reference, revealing diverse progenitor populations giving rise to excitatory and inhibitory neural lineages, and subsets of maturing neurons (Fig. 3b,c and Extended Data Fig. 5d-f).

Given the migratory and functional deficits in 15q13.3del MGE-like inhibitory neurons (MGE-InhibNs), we focused on this subpopulation in our spatial analysis. We first applied Nearest Neighbor Analysis[82] to probe the local MGE inhibitory neuron network and identified neighboring cell types throughout the assembloid tissue. We found a lower proportion of 15q13.3del MGE-InhibNs were localized next to excitatory neurons (Fig. 3d) and were instead adjacent to GE NPCs, adding context to the migration deficits we previously identified (Fig. 2c).

To better understand the influence of cell localization in these interactions, we examined the transcriptome of migrated and stationary MGE-InhibNs in context to the dorsal-ventral border (Fig. 3e). To do this analysis, we constructed spatial annotations around the dorsal tissue using the SPATA2 package and canonical MGE lineage markers (Extended Data Fig. 5g)[83]. Our comparison between migrated and stationary MGE-InhibNs within control and 15q13.3del tissues revealed numerous DEGs, roughly 75% of which are shared between genotypes, including the transcription factor *SP8* (1.29-fold increase in migrating control MGE-InhibNs, 2.79-fold increase in 15q13.3del migrating MGE-InhibNs) and reductions to neurogenesis-associated genes HES1[84] and ASCL1[85,86].

A small subset of 25 genes (Fig. 3f) exhibited an inverse expression pattern; these genes were upregulated in migratory control MGE-InhibNs but downregulated in stationary 15q13.3del MGE-InhibNs. This gene set included cell adhesion molecule and axon guidance genes NECTIN1 and ROBO1. The gene set was also enriched in pathways relating to the signaling and synaptic transmission of GABA, a critical inhibitory neurotransmitter (Fig. 3g). Comparing migrated MGE-InhibNs between genotypes, identified reductions to gene modules pertaining to interneuron migration (Fig. 3h) and GABAergic synapses (Fig. 3i), including genes such as the GABA synthesizer GAD1 and receptor, GABRA2 (Fig. 3i). These data suggest that despite entering the dorsal microenvironment, 15q13.3del MGE-inhibitory neurons have signaling defects and may not participate as efficiently in neural circuits.

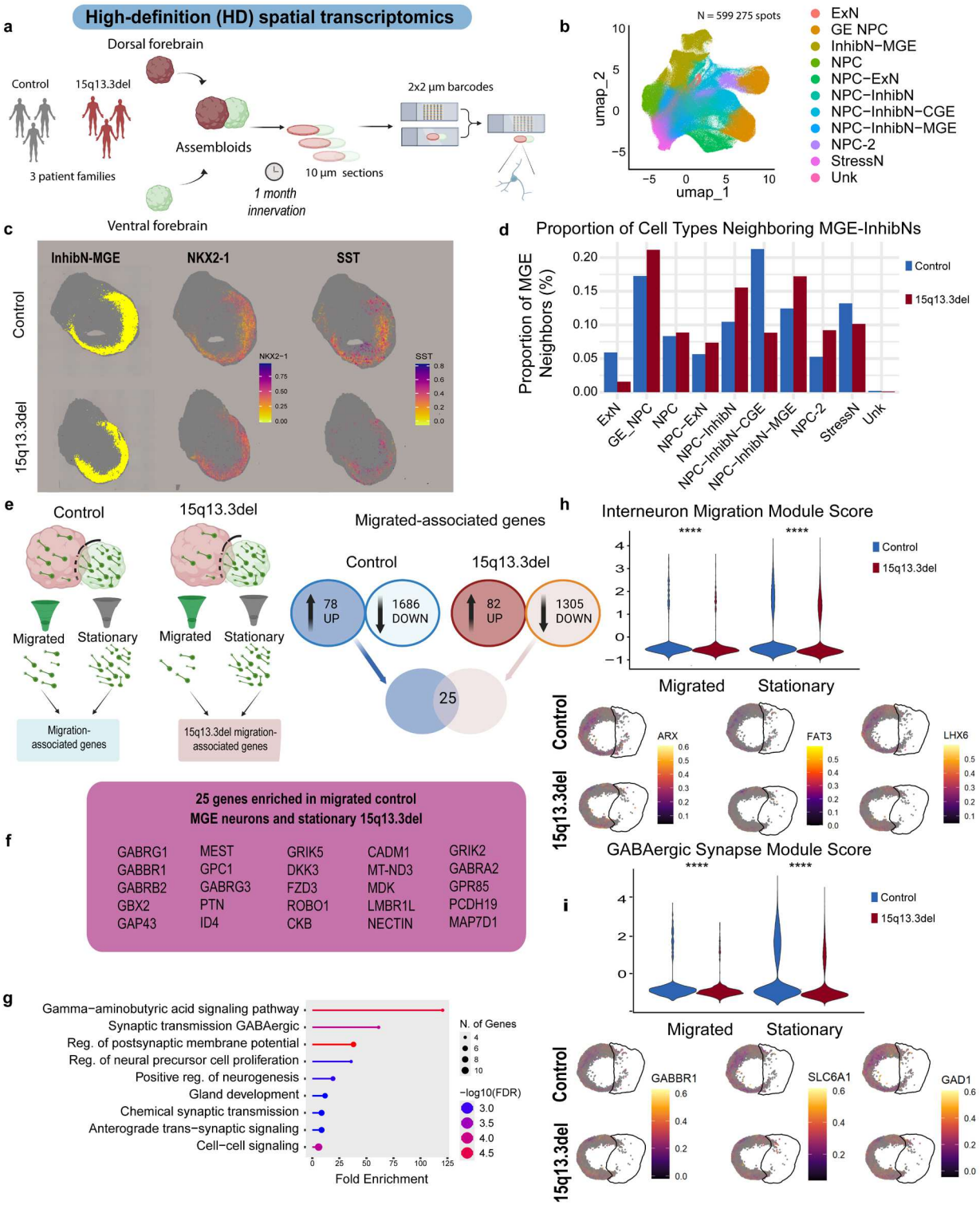


Fig. 3: High-definition spatial transcriptomics captures migration-dependent deficits and spatially defined transcriptional changes amongst 15q13.3del inhibitory neurons.

a, Sample preparation of N = 3 families for high-definition (HD) Visium spatial transcriptomics. **b,** UMAP plot of Visium HD dataset with annotated cell types, n = 599 275 spots. **c,** MGE-InhibNs localization and canonical marker expression in forebrain assembloid tissue. **d,** Proportion of unique cell types neighboring MGE-InhibNs (Semla, Find region neighbors function)[82]. **e,** Schematic for MGE-InhibNs migration analysis depicting genotype- and regionally defined subpopulations. Venn diagram lists migration-related genes comparing stationery to migrated MGE-InhibNs within genotypes. Control n = 1387 DEGs, 15q13.3del n = 1764 DEGs. **f,** List of 25 genes enriched in migrated (control) and stationary (15q13.3del) MGE-InhibNs. **g,** Top 10 GO enrichment terms amongst inverse migration-associated genes (FDR < 0.05). **h-i,** violin plots of module scores for interneuron migration and GABAergic signatures amongst MGE-InhibNs stratified by migration status. Interneuron migration module: migratory MGE-InhibN pAdj = 8.200e-19,

stationary MGE-InhibN pAdj < 1e-308, GABAergic synapse module: migratory MGE-InhibN pAdj = 5.24e-23, stationary MGE-InhibN pAdj < 1e-308. Control *vs* 15q13.3del module expression comparisons were performed within each subset using Wilcoxon rank-sum tests, and p-values were adjusted for multiple testing with the Benjamini–Hochberg method.

Functional deficits in 15q13.3del inhibitory neurons in human forebrain assembloids and mice.

The early deficits in inhibitory neuron migration and maturation in 15q13.3del assembloids prompted us to test whether these cells exhibit broad functional impairments. We used the calcium indicator pAAV-mDlx-GCaMP6f-Fishell-2 to label inhibitory neurons within our assembloid tissue to record spontaneous calcium events at 5 months of development, a stage reflecting functional neuronal maturation[71–73] (Fig. 4a). To ensure the spontaneous changes in GCaMP6f fluorescence ($\triangle F/F_0$) in assembloids were calcium-dependent and associated with action potential firing, assembloids were treated with a calcium chelator BAPTA (30 μM) and a sodium channel blocker tetrodotoxin (TTX, 0.5 μM), respectively. As expected, each treatment resulted in a loss of calcium transients and synchronous network activities (Supplementary Video 1-4). Quantification of single-neuron calcium dynamics (see **Methods**)[74] revealed a significant reduction in the frequency of calcium transients of single inhibitory neurons (Fig. 4b,c), suggesting general inhibitory hypoactivity in 15q13.3del forebrain assembloids.

To isolate MGE-derived inhibitory neurons exclusively, we labelled single ventral organoid tissue with the same virus prior to fusion with dorsal organoids, enabling circuit maturation and integration within the assembloid (Fig. 4d). Consistent with the pan-inhibitory neuron recordings, we detected reductions to the average frequency of Dlx5+ inhibitory neurons derived from the ventral organoid (Fig. 4e,f).

We next asked whether inhibitory neuron dysfunction observed in human 15q13.3del models was conserved *in vivo* using the Df(h15q13)/+ mouse, which recapitulates many of the clinical and biochemical pathologies observed in patients[30,31,54,75]. We targeted putative inhibitory neurons in the medial prefrontal cortex (mPFC) of adult Df(h15q13)/+ mice, specifically layer II/III (Fig. 4g), as this region is highly populated by parvalbumin and somatostatin interneurons derived from the MGE[76,77]. Using postnatal tissue, we identified a reduction in inhibitory neuron excitability in response to increasing current steps (Fig. 4h,i). To determine if the hypoexcitability influenced E/I circuit development, we targeted putative layer V pyramidal excitatory neurons and found reductions in both the frequency and amplitude of spontaneous inhibitory post synaptic currents (sIPSCs) (Fig. 4j,k). These findings indicate that interneuron dysfunction persists in the mature Df(h15q13)/+ cortex, mirroring the inhibitory deficits observed in patient-derived assembloids and aligning with prior evidence implicating interneuron pathology in neurodevelopmental disorders [78,79].

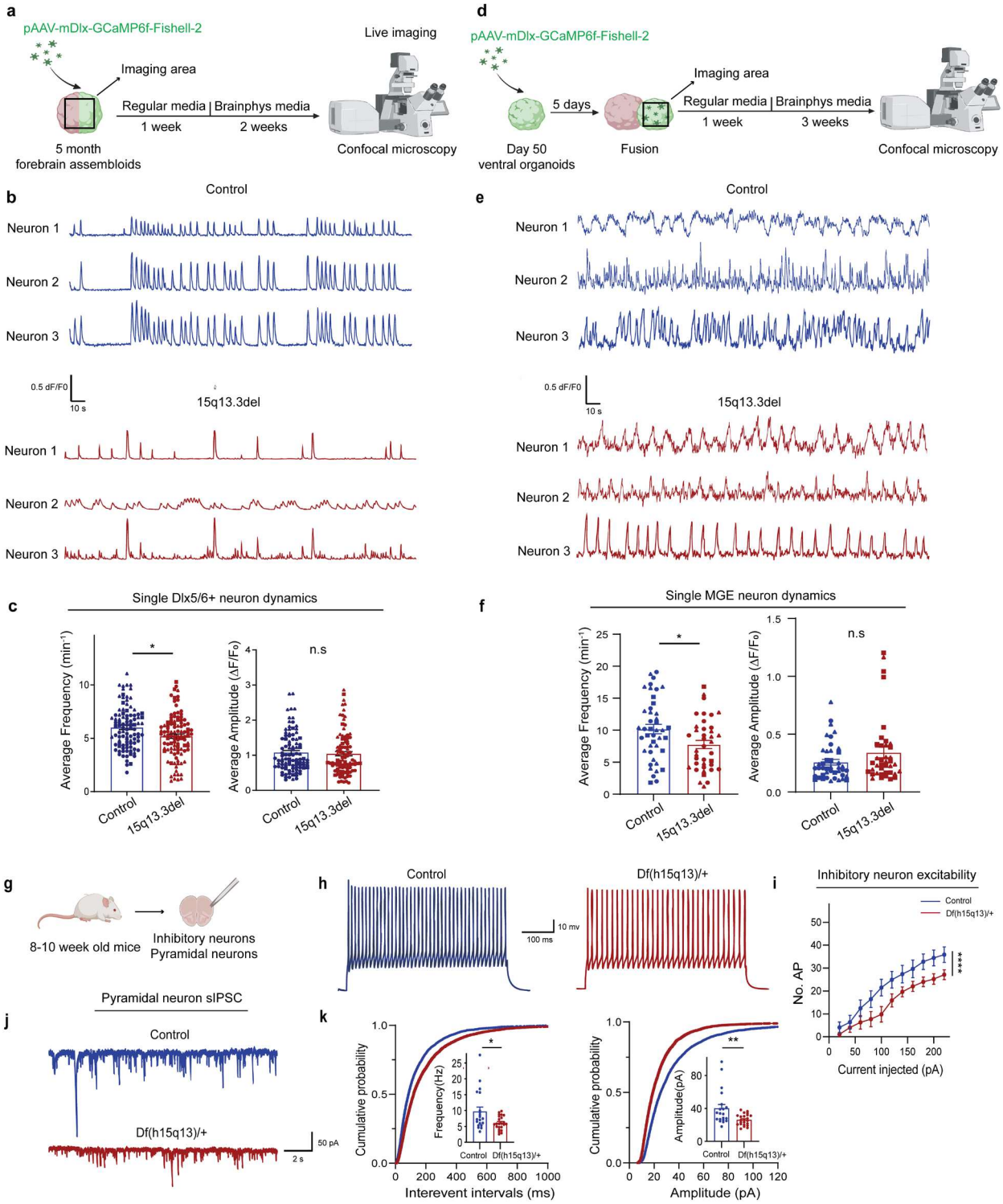


Fig. 4: 15q13.3del Inhibitory neuron hypoactivity is conserved across species.

a, Calcium imaging labeling strategy for mature pan-inhibtory neuron recordings. **b-c,** Representative calcium traces from pAAV-mDlx-GCaMP6f-Fishell-2 live calcium imaging protocol of 5-month forebrain assembloids and quantification of single neuron dynamics from N = 3 families, control n = 87 field of view (FOV) recordings across 18 assembloids, 15q13.3del n = 90 FOVs across 20 assembloids. **d,** Calcium imaging labeling strategy for ventrally-derived Dlx5/6+ inhibitory neuron recordings. **e-f,** Representative calcium traces from pAAV-mDlx-GCaMP6f-Fishell-2 live calcium imaging protocol of 3-month-old forebrain assembloids and quantification of single neuron dynamics from N = 3 families, control n = 43 neurons across 14 assembloids, 15q13.3del n = 39 neurons across 10 assembloids. **g-k,** Patch clamp electrophysiology of adult control and Df(h15q13)/+ medial prefrontal cortex (mPFC). **h-i,** Representative action potential traces and firing properties in layer II/III mPFC inhibitory neurons generated by current injection (–200 pA - +220 pA pA, 100 ms). n = 13 cells from 6 control mice (2 females, 3 males), n = 10 cells from 4 Df(h15q13)/+ mice (2

females, 2 males). **j,** Representative spontaneous IPSCs (sIPSCs) traces recorded from layer V pyramidal excitatory neurons from control and Df(h15q13)/+ mice. **k,** Cumulative distribution and quantification of frequency and amplitude of sIPSCs. n = 20 cells from 6 control mice (2 females, 4 males), n = 23 cells from 6 Df(h15q13)/+ mice (2 females, 4 males). Error bars represent mean ±SEM in assembloids; *p<0.05, **p<0.01, ***p<0.001.

15q13.3del forebrain assembloids display hyperactive neuronal calcium dynamics and synaptic hyperconnectivity

Given the developmental and functional deficits amongst inhibitory neurons in our mouse and human 15q13.3del models, we asked whether this led to global neural circuit disruptions in assembloid tissue. We infected excitatory neurons in dosal organoids using pENN.AAV.CamKII.GCaMP6f.WPRE.SV40, followed by fusion with ventral organoid to make assembloids. This allowed us to examine calcium activity (as a proxy for neuronal activity) across excitatory neurons in forebrain assembloids at 3 months of development (Fig. 5a). We observed increases in the frequency and amplitude of calcium events in single excitatory neurons (Fig. 5b,c), as well as in the frequency and amplitude of synchronous network events (Fig. 5d) amongst excitatory neural populations, suggestive of a hyperactive phenotype.

Calcium signals provide information about neuronal depolarizations[93] but do not provide insight to synapse formation, which is required for neural circuit formation and function[94]. To assess the synaptic connectome in maturing forebrain assembloids, we performed monosynaptic rabies tracing[69] in 5-month forebrain assembloids using RABV-EnvA-deltaG-GFP-F2 and a non-cell type-specific helper virus (AAV-CMV-TVA-mCherry-2A-oG) (Fig. 5e). We quantified the connectivity ratio as the proportion of presynaptic/postsynaptic neurons and found a total increase throughout the assembloid tissue (Fig. 5f)[70]. Together, these results suggest that in the 15q13.3del condition, inhibitory neurons have reduced connectivity and function, which may drive elevated calcium activity and overall hyperconnectivity in excitatory neurons.

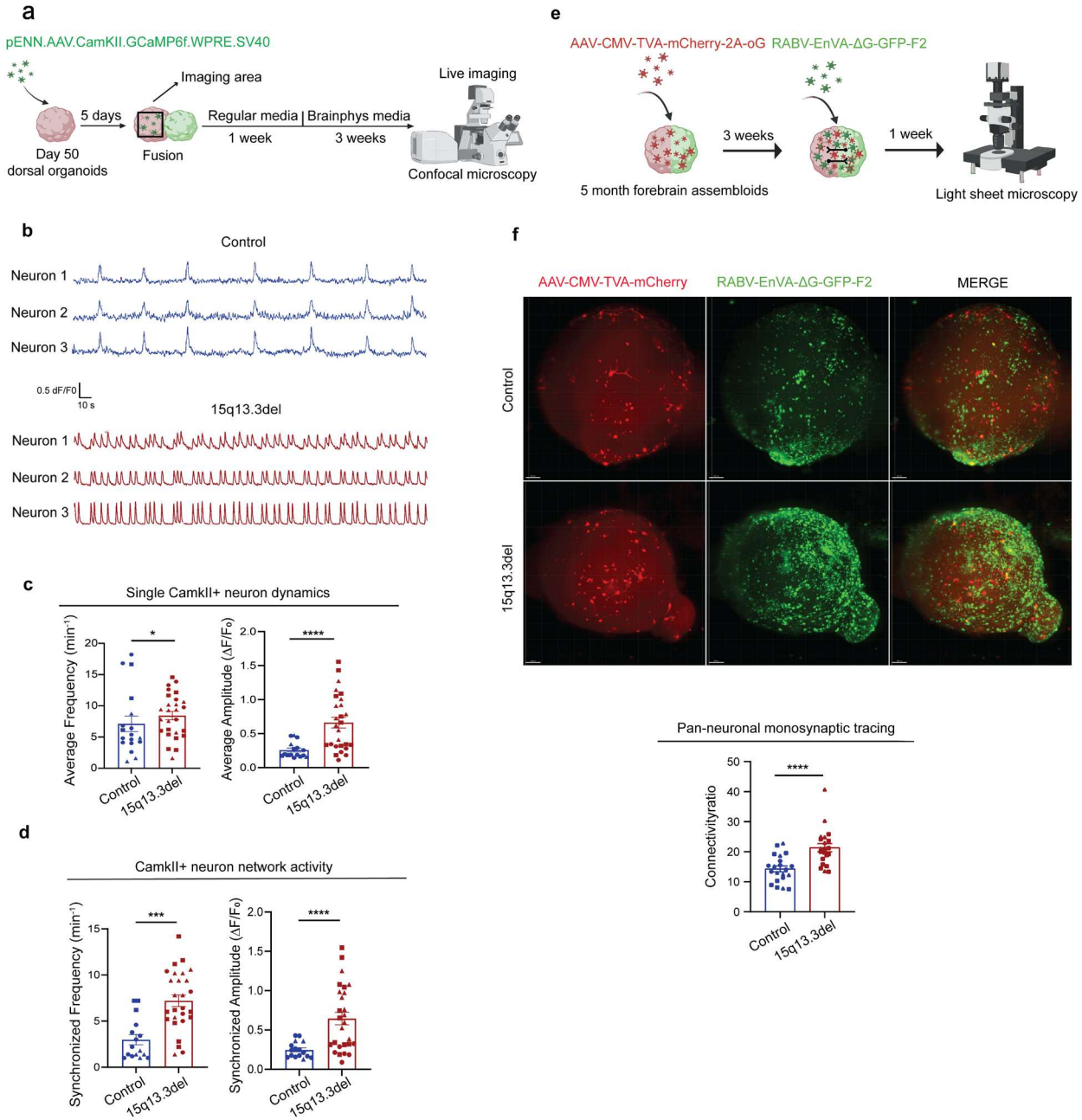


Fig. 5: 15q13.3del forebrain assembloids display neural hyperactivity and hyperconnectivity.

a, Calcium imaging labeling strategy for dorsally-derived CAMKII+ excitatory neuron recordings within assembloids. **b,** Representative calcium traces from pENN.AAV.CamKII.GCaMP6f.WPRE.SV40. live calcium imaging protocol of 3-month-old forebrain assembloids. **c,** Average frequency and amplitude of calcium events in single neurons and **d,** network synchronous events frequency and amplitude in N = 3 families, control n = 18 FOV recordings, 15q13.3del n = 27 FOVs, across 11 assembloids per genotype. **e,** Rabies monosynaptic tracing strategy for unbiased labelling of pan-neuronal synaptic connectomes in 5-month old forebrain assembloids. **f,** Representative 4x IMARIS images of 5-month assembloid infected with AAV-CMV-TVA-mCherry and quantified connectivity ratio of synaptically connected neurons. N = 3 families, n = 21 assembloids per genotype. Scale bars represent 400 µm. Error bars represent mean ±SEM in assembloids; *p<0.05, **p<0.01, ***p<0.001.

Elevated FAN1-related DNA damage is present in 15q13.3del MGE inhibitory neurons

To study the potential mechanisms underlying the functional and spatial deficits observed in 15q13.3del assembloids, we probed our spatial transcriptomics data for possible mediators of these deficits. We considered that amongst the differentially expressed genes in our bulk, single cell- and spatial transcriptomics datasets, FAN1 and KLF13 were consistently the highest of those within the 15q13.3 locus, both within single organoids and in assembloid tissue (Fig. 6a). We focused on FAN1 since this gene has been previously associated with schizophrenia[90] and our initial bulk RNAseq data indicated DNA-related mechanisms (Fig. 1b). *FAN1* encodes a DNA repair nuclease that is highly associated with DNA damage and neurodegeneration[87–89], but its role in neurodevelopment is unexplored. We screened the Visium HD dataset for DNA damage-associated pathways and identified signatures enriched across different neural cell populations (Fig. 6b). These GO terms were broad (including DNA- and double-stranded break repair amongst multiple cell types) and also more specific to FAN1, including an enrichment for interstrand crosslink repair (ICR) amongst MGE-InhibNs (2.24– fold enrichment, Fig. 6b) for which FAN1 is a key regulator[91,92]. Given the impaired inhibitory neuron migration and different spatial transcriptomic profiles of migrated and stationary MGE-InhibNs, we further examined the DNA damage-associated gene modules in migrated and stationary MGE-InhibNs and found that the ICR signature was disrupted in both neuron populations, although a higher proportion of stationary neurons expressed the ICR damage signature (Fig. 6c).

Likewise, we identified more generalized enrichment for DNA damage amongst the MGE-InhibNs within both migratory groups (Fig. 6d). To validate the enrichment of DNA damage at the protein level, we used age-matched assembloids and probed for the canonical DNA damage marker phospho-γ-H2AX foci (Fig. 6e). We identified an increase in the total phospho-γ-H2AX foci in 15q13.3del nuclei, which we further probed in Dlx5+ inhibitory neurons and showed that inhibitory neurons specifically produced DNA damage signatures (Fig. 6f). We next profiled DNA breaks in individual cells within ventral forebrain organoid tissue using the neutral COMET assay, which uses electrophoresis to detect DNA damage at the single cell level (Fig. 6g). We found increased tail moment and length in 15q13.3del cells, demonstrating primarily double-strand DNA breaks. Together, these data suggest that inhibitory neuron deficits begin at early stages and include alterations to DNA damage/repair mechanisms, which may cause subsequent functional deficits observed in these subpopulations.

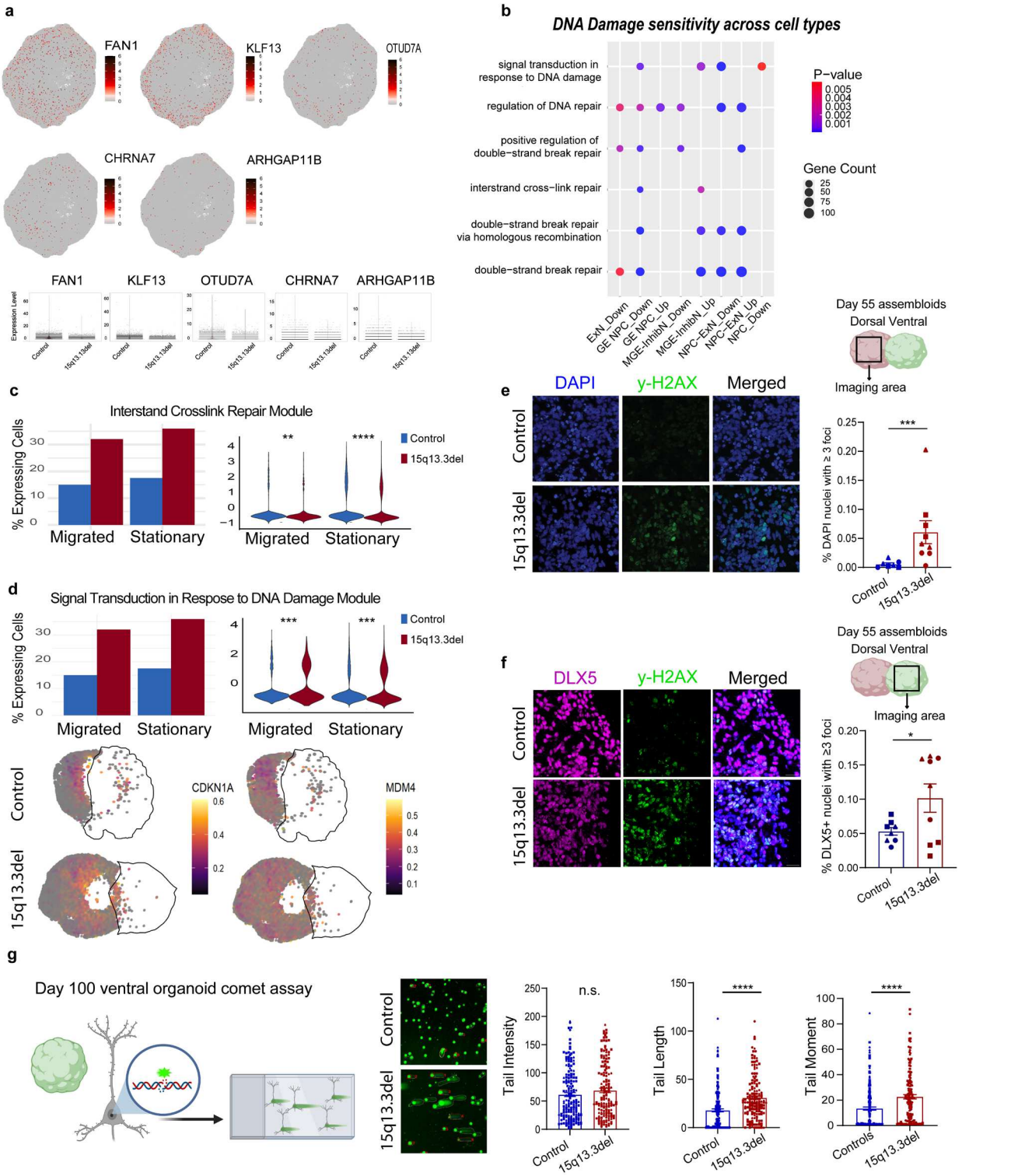


Fig. 6: 15q13.3del assembloids display inhibitory neuron-specific DNA Damage that is captured at the single cell level.

a, 15q13.3 gene expression and spatial localization in day 55 forebrain assembloid tissue. **b,** Select DNA Damage GO terms amongst forebrain assembloid cell types (FDR < 0.05). **c,** Proportion of cells expressing and total module scores for interstrand crosslink signatures amongst MGE-InhibNs stratified by migration status (migratory MGE-InhibN pAdj = 2.2e-03, stationary MGE-InhibN pAdj = 3.4e-259). **d,** Proportion of cells expressing and total module scores for DNA damage signal transduction signatures amongst MGE-InhibNs stratified by migration status (migratory MGE-InhibN pAdj = 0.00043, stationary MGE-InhibN pAdj = 0.00018). Control *vs* 15q13.3del module expression comparisons were performed within each subset using Wilcoxon rank-sum tests, and p-values were adjusted for multiple testing with the Benjamini–Hochberg method. **e,** Phospho-γ-H2AX immunocytochemistry in day 55 assembloid tissue quantifying the proportion of cells with three or more foci. N = 3 families, control n = 6 organoids, 15q13.3del n = 7 organoids. **f,** Phospho-γ-H2AX signal enrichment in day 55 Dlx5+ inhibitory neurons. N = 3 families, control n = 8 organoids, 15q13.3del n = 9

organoids. **g,** COMET assay of 3-month-old ventral tissue and quantified DNA fragmentation. N = 3 families, control n = 169 cells across 6 organoids, 15q13.3del n = 150 cells across 6 organoids. Error bars represent mean ±SEM in assembloids; *p<0.05, **p<0.01, ***p<0.001, ***p<0.0001.

Discussion

Human brain assembloids are powerful models for uncovering early disease mechanisms for neurodevelopmental and neuropsychiatric disorders. Moreover, because these conditions arise from the interplay of diverse and developmentally-sensitive cell types, it is critical to understand disease processes in a cell type–specific and regionalized manner. Here we leveraged patient-derived forebrain assembloids to model the recurrent 15q13.3 microdeletion disorder, utilizing single cell and spatial transcriptomic approaches in combination with functional assays to identify pathogenic mechanisms in excitatory and inhibitory neuron lineages. Our study revealed that early impairments in migration and synapse formation within specific subpopulations of human inhibitory neurons were linked to FAN1-associated DNA damage repair, which likely contributed to later hyperconnectivity phenotypes in assembloids. These findings point to early disruption of inhibitory neuron genomic integrity and DNA repair capacity as an early pathogenic driver, which together with excitatory neuron dysfunction, may drive circuit-level hyperconnectivity and hyperactivity characteristic of the 15q13.3 microdeletion–associated neurodevelopmental disorder.

The 15q13.3 microdeletion, like other CNVs at 16p11.2, 22q11, and 3q29, are common CNVs for which organoid and assembloid models are beginning to reveal new insight into human neurodevelopmental disease pathology[3,5,95,96]. We and others have previously shown in 15q13.3del mouse models and patient iPSC-derived neurons that CHRNA7 and OTUD7A mediate pathogenic defects in excitatory neurons in the postnatal brain [30–32,50–55]. However, CNVs involve multiple genes expressed across distinct developmental windows, underscoring the importance of assembloids for modeling prenatal mechanisms. We found that CHRNA7 and OTUD7A are weakly expressed at multiple timepoints, whereas FAN1 and KLF13 are robustly expressed. KLF13 is a transcription factor that is best known for its role in early cardiac development[97] and regulates mouse interneuron progenitor proliferation in an isogenic model[79]; therefore, KLF13 could also contribute to human inhibitory neuron development given its expression[98].

Our multi-omic analysis uncovered enriched DNA damage and repair signatures in migrating MGE-like inhibitory neurons within 15q13.3del assembloids (Fig. 6c,d). Elevated γ-H2AX levels were detected in both dorsal forebrain tissue and Dlx5+ ventral inhibitory neurons derived from 15q1313.del assembloids (Fig. 6e,f), while mature ventral organoids showed increased global DNA damage (Fig. 6g). These findings are consistent with FAN1 haploinsufficiency and its established role in interstrand crosslink repair[127-128]. We propose that FAN1 haploinsufficiency-mediated DNA repair defects shape early, cell type-specific vulnerabilities during fetal brain development, prior to the postnatal disease mechanisms. Impaired DNA repair may disrupt the ability to elicit downstream transcriptional programs necessary for the early stages of neural circuit formation, including activity dependent signaling pathways that coordinate neuronal maturation and synapse function[103–105]. Given the role of FAN1 in expansion repeats, it will be important to examine whether haploinsufficiency drives triplet repeat expansion in the 15q13.3del genome, potentially adding transcriptional complexity during brain development[106].

Assembloids have emerged as a promising tool to model complex cell-cell interactions and circuit biology in the context of both typical development and disease pathology. [10, 129-132]. In this study, we paired assembloid neural circuits phenotyping with unbiased spatial transcriptomics at single cell resolution to identify spatially restricted, cell type-specific disease mechanisms. This integrative platform enabled the direct visualization of migrating, transcriptionally perturbed inhibitory neurons and progenitors *in situ,* revealing a DNA damage signature disrupting the early stages of neural circuit development[90–93]. While previous human organoid studies using spatial transcriptomic technologies such as the 10x Genomics Xenium have advanced our understanding of the cellular composition of these model systems[107–110], their reliance of biased, pre-determined probes can limit the identification of unanticipated cell types and signaling networks within the heterogeneous tissue. We anticipate further use of unbiased, whole-transcriptome spatial

platforms in assembloids to explore previously unknown aberrant signaling networks that disrupt human tissue development and cause disease.

In summary, our study demonstrates how human brain assembloids, spatial transcriptomics, and functional analyses can uncover early cell type–specific mechanisms of neural circuit disruption. By uncovering a role for FAN1-associated DNA repair in early inhibitory neuron lineages, our findings provide new biological insight into inhibitory neuron development and highlight the potential for this platform to be applied across diverse NDD models to identify early biomarkers and therapeutic opportunities.

Limitations of the study

While unbiased spatial biology approaches combined with functional neural assays offer powerful tools to explore NDD pathophysiology, there are limitations to our study. First, the optimization of the HD platform for assembloids requires 10 µm tissue sections, which captures a fraction of the inherently complex assembloid system and is therefore influenced by the tissue heterogeneity. We also encountered lower UMI counts in the center of the assembloids which may be a biological artifact caused by limited access of cells in the core to nutrients during assembloid growth, adding to variability[111–113]. Although our spatial transcriptomic findings were generated across 3 independent 15q13.3del families, future studies may need to analyze multiple tissue sections per assembloid to reduce variability. In addition, future studies on the 15q13.3del CNV should address the molecular mechanisms by which FAN1-mediated DNA repair/damage contribute to transcriptional abnormalities in developing neural circuits, as well as whether inhibition of these pathways will rescue E/I neural circuit deficits. Taken together, our findings show that combining neural functional assays with spatial transcriptomics in assembloids offers a powerful platform to uncover previously unrecognized cell types and early signaling pathways of NDD states.

Methods

hiPSC Reprogramming and maintenance.

Patient sample collection and Cell Oversight Committees.

All pluripotent stem cell work was approved by the Stem cell oversight committee (SCOC) from the Canadian Institutes of Health Research. Blood samples were collected from individuals with the approval from SickKids Research Ethics Board after informed consent was obtained (REB approval file #1000050639). Additionally, this study was approved by the University Health network REB #21-5860 the Hamilton Integrated Research Ethics Board, (REB approval file #2707). Fibroblast and blood samples were acquired from locations globally and are outlined per family/sample (Table 1).

Table 1: Clinical presentations and background of patients heterozygous for the 15q13.3 microdeletion.

Patient ID	Sex	Proband relation	Clinical presentations	Deletion size (kbp)
Family 1 control	Female	Mother	Neurotypical	No 15q breakpoints
15q13.3del Patient 1	Female		ASD	1530.69
Family 2 control	Male	Brother	Neurotypical	No 15q breakpoints
15q13.3del Patient 2	Female		Epilepsy (absence seizures), DD, ID	2000.669
Family 3 control	Male	Father	Neurotypical	No 15q breakpoints
15q13.3del Patient 3	Female		Severe epilepsy (absence seizures), ADHD, ASD	1348.142
Family 4 control	Female	Mother	Neurotypical	No 15q breakpoints
15q13.3del Patient 4	Female		Epilepsy (myoclonic absence seizures), abnormal EEG and MRI, thick corpus callosum	1533.257
Family 5 control	Female	Mother	Neurotypical	No 15q breakpoints
15q13.3del Patient 5	Female		DD, Thick corpus callosum, T2 hyperintensity in tegmental tracks, language and motor delay	2060.432
15q13.3del Patient 6	Female	No familial control	Global DD and ID	3063.946

ADHD - attention deficit hyperactivity disorder, ASD - Autism spectrum disorder, DD - developmental delay, EEG – Electroencephalography, ID - Intellectual disability, kbp - kilobase pairs.

Table 2: hiPSC line allocation per experiment

Experiment	Family lines used	Batch replicates	Timepoint(s)
Forebrain organoid bulk transcriptomics	1-5	3 technical replicates per timepoint	Day 50 and 100
Forebrain organoid scRNA Seq	2, 3, 5	2 batch families 3 and 5, 3 batches family 2	Day 100
Ventral organoid SST/NKX2-1 IF	2, 3, 5	1 batch	Day 50
Forebrain assembloid DLX5+ γH2AX IF	2, 3, 5	1 batch	Day 55
Forebrain assembloid dorsal side γH2AX IF	2, 3, 5	1 batch	Day 55
Ventral organoid neutral comet assay	2, 3, 5	1 batch	Day 100
Forebrain assembloids migration assay	2, 3, 5	1 batch	Day 55
Forebrain assembloid CMV rabies	2, 3, 5	1 batch	5-month
Forebrain assembloid Dlx5/6 rabies	2, 3, 5	1 batch	5-month
Forebrain assembloid Dlx5/6 calcium imaging	2, 3, 5	2 batches for family 3	5-month
Forebrain assembloid MGE calcium imaging	2, 3, 5	1 batch	Day 90
Forebrain assembloid CAMKII calcium imaging	2, 3, 5	1 batch	Day 90
Forebrain assembloid 10x Visium HD spatial transcriptomics	2, 3, 5	1 batch	Day 55

Patient cohort

Patients heterozygous for the 15q13.3 microdeletion were consented and collected at sites across Canada, the United States, and Italy. Microarray data determined that the deletions ranged from 1.5-2Mb in size. Clinical assessments were provided upon request and revealed a heterogeneous population of individuals with ASD, intellectual disability, and epilepsy, most often presenting with absence seizures. Information on clinical background and deletion size for our cohort can be found in Table 1.

Reprogramming and hiPSC culturing.

$CD34^+$ blood cells were assessed via flow cytometry and collected for iPSC reprogramming. iPSCs from Family 1 and 2 were reprogrammed by the Centre for Commercialization of Regenerative Medicine (CCRM, MaRS Centre, Toronto, ON, Canada) and iPSCs from families 3-6 were generated *in-house*. iPSCs were generated by Sendai viral reprogramming and clonal expansion using the CytoTune – iPSC 2.0 kit (Thermo Fisher) according to manufacturer instructions. In brief, colonies were expanded for 2-3 weeks, and once large enough were transferred to a single well of a 12-well plate coated with irradiated mouse embryonic fibroblasts. iPSC media consisted of DMEM/F12 supplemented with 10% KO serum, 1× non-essential amino acids, 1× GlutaMAX, 1 mM β-mercaptoethanol, and 16 ng/mL basic fibroblast growth factor. After expansion, iPSCs were grown on Matrigel-coated 6-well plates in mTeSR1 (STEMCELL Technologies), where all subsequence passaging was performed with ReLeSR (STEMCELL Technologies). Line validation was performed with flow cytometry and immunocytochemistry of pluripotency markers (Extended Data Fig. 1f and Fig. 1f)., and cytogenomic karyotyping was assessed via G-Banding analysis at The Centre for Applied Genomics (TCAG, SickKids, Toronto, ON, Canada). CNV microarray calling was performed using the CytoScan HD array using standard settings of ChAS, which looks for copy number differences of at least 50 markers and 400 kbp (TCAG, SickKids, Toronto, Canada). Data for hiPSC validations can be found in Extended Data Fig. 1. Routine mycoplasma screens were performed using the EZ-PCR™ Mycoplasma Detection kit (Froggabio) under manufacturer's guidelines (Extended Data Fig. 1e). Images were taken on a BioRad ChemiDoc imaging system.

Organoid and assembloid generation

Forebrain neural organoids were generated with the STEMdiff ™ Dorsal/Ventral Forebrain Organoid kits from STEMCELL Technologies™ using low-passage (P20-P30) hiPSCs under the manufacturer instructions. Assembloids were generated from dorsal and ventral forebrain organoids on day 25 or day 55 of differentiation; using a wide-bore P1000 pipette tip, individual organoids from dorsal and ventral lineage were placed into one ultra-low attachment U-bottom 96 well plate (Corning) in 200 µL of media. Plates were then centrifuged for 15 seconds on a "quick spin" setting. A half media change was performed the following day, and on day 4 assembloids were moved into a 6 well ultra-low attachment plate (Corning) using a wide-bore P1000 tip.

Organoid fixation and immunocytochemistry

Organoids were washed 3x in Phosphate Buffered Saline (PBS) for 10 minutes prior to a 48-hour fixation in 4% paraformaldehyde (PFA). Samples were dried in 30% and then 50% sucrose in PBS overnight and then embedded in either Optimal Cutting Temperature (OCT) (1-month unguided neural organoids) or gelatin (all other samples) and stored at -80℃. Sections were made on the Leica CM3050S at 20 µm on SuperFrost™ Plus microscopy slides and stored at -30℃. The slides were washed 3x in 1x Phosphate Buffered Saline supplemented with Tween-20 (PBS-T) and incubated in a blocking/permeabilization solution comprised of 10% Donkey serum (Millipore) and 0.03% Triton X-100 (Fisher Scientific) in PBS for 1 hour at room temperature. Samples were incubated in this solution with primary antibodies overnight at 4℃. Samples were washed 3x with 1x PBS-T, followed by a 2-hour incubation at room temperature with secondary antibodies. Samples were washed 2x with 1x PBS-T, incubated with DAPI nuclear dye for 15 minutes, followed by a final wash with 1x PBS-T. Samples were mounted on Vista Vision glass microscope slides (VWR) using Prolong Gold antifade reagent (Life Technologies).

Confocal microscopy and ICC cell population analyses

Confocal Z-stack images were taken on a Zeiss LSM 800 with a 2048x2048 resolution. Images were processed with ImageJ 1.44 Software (Fiji) and analyzed using CellProfiler 4 (BMC Bioinformatics). For population analyses, manual regions of interest (ROIs) were drawn, and maximum intensity projections of each channel were processed and a threshold applied to report cell populations normalized to $DAPI^+$ nuclei (unless otherwise stated).

Lentiviral labeling of iPSCs for neuronal migration assay in assembloids

iPSCs were seeded at a density of 250 000 cells/6 well and supplemented with Y-27632 ROCK Inhibitor (1: 1 000 STEMCELL Technologies™). The following day lentivirus harboring FUW-hSYN-M2rTTA was added at 1: 24 000 dilution in addition to 1: 5 000 of either pTET-O-CMV- mCherry (for lines intended for dorsal differentiation) or pTET-O-CMV-eGFP (ventral differentiation) to conditioned media supplemented with polybrene (1: 20 000, of 10 mg/mL stock, Sigma) and Y-27632 ROCK Inhibitor (1: 1 000) (Extended Data Fig. 4a,b). To profile ventral inhibitory neuron migration into dorsal organoids, the iPSCs labelled with mCherry and eGFP were used to generate dorsal and ventral organoids respectively. Next, $eGFP^+$ ventral organoids were fused with $mCherry^+$ dorsal organoids at day 25, and four types of assembloids were generated by fusing organoids of each genotype to study cell-autonomous and non-cell-autonomous effects (Fig. 2b). 25 days post-assembly (day 55 of differentiation), maturation media was supplemented with 1 µg/mL of doxycycline to induce expression of fluorophore constructs. Induction proceeded for five days, after which the assembloids were fixed in 4% PFA and processed for immunocytochemistry or tissue clearing and light sheet microscopy.

Tissue clearing (CUBIC Protocol) and light sheet microscopy

Fixed samples were processed using the CUBIC protocol[114] with minor modifications based on organoid and assembloid size. Briefly, fixed assembloid samples were incubated overnight at room temperature with the nuclear stain RedDot 647 (Biotrend, 1:100, shaking at 350 RPM), followed by three 1x PBS washes. Samples were incubated in 50% CUBIC-1 in H_2O for 2 hours at 37℃, followed by a 48-hour incubation with 100% CUBIC-1 at 37℃. Samples were washed 3x with 1x PBS for 30 minutes and then incubated in 50% CUBIC-2 for 3 hours, followed by an overnight incubation in 100% CUBIC-2 at 37℃. Samples were washed in type FF immersion oil (16212, Cargille Laboratories Inc. Cedar Grove, NJ, USA) for 10 minutes at room temperature prior to imaging.

Light sheet imaging was performed using the Ultramicroscope II light sheet microscope (LaVision BioTec GmbH, Bielefeld, Germany) at 4× magnification to capture the entire assembloid using 2× artificial zoom, 40% sheet width, 5 µm thickness, 1 µm z stack size. Images were exported into 16-bit IMS files on IMSpector and analyzed with IMARIS software (V10.0.0, Bitplane Inc. Zurich, Switzerland) and the proportion of $hSYN\text{-}eGFP^+$ ventral neurons was quantified using the Spots tool and Chi sum of squares statistical test for cell nuclei identification. We chose to report the proportion

of cells migrating rather than raw values to mitigate confounding variables caused by differences in labeling efficiencies between cell lines.

Patch clamp electrophysiology

Slice preparation

Mice were anesthetized with isoflurane and the brain was quickly removed and placed in ice-cold cutting solution, consisting of the following (in mM) 92 NMDG, 2.5 KCl, 1.25 NaH2PO4, 30 NaHCO3, 20 HEPES, 25 glucose, 2 thiourea, 5 Na-ascorbate, 3 Na-pyruvate, 0.5 CaCl2·2H2O, and 10 MgSO4·7H2O. Titrate pH to 7.3–7.4 and osmolarity of 295–300 mOsmol/L. Coronal mPFC slices were cut to a thickness of 300 µm using a vibratome (Leica VT 1200). The slices were transferred to HEPES holding aCSF (in mM): 92 NaCl, 2.5 KCl, 1.25 NaH2PO4, 30 NaHCO3, 20 HEPES, 25 glucose, 2 thiourea, 5 Na-ascorbate, 3 Na-pyruvate, 2 CaCl2·2H2O, and 2 MgSO4·7H2O. Titrate pH to 7.3–7.4 at 32C for 15 minutes, and then transferred to artificial cerebrospinal fluid (aCSF) for a minimum of 45 minutes, containing the following (in mM): 126 NaCl, 2.5 KCl, 1.25 NaH2PO4, 1.5 MgCl2, 2.5 CaCl2, 26 NaHCO3, and 10 glucose, with pH 7.3–7.4 and osmolarity of 295–300 mOsmol/L. All the solutions were saturated with 95% O2 and 5% CO2.

Whole-cell patch clamp recordings

During recordings, individual slices were placed in a submersion chamber and perfused with aCSF at a rate of 1.5-2 ml/min at 30-32°C. mPFC slices were observed using an upright microscope (Olympus U-TV1XC) equipped with a water-immersion long-working distance objective (40x; differential interference contrast, DIC) and an infrared CCD camera (DAGE-MTI IR-2000). In accordance with the known morphology of interneurons and their firing properties, cells with small and round soma shapes were selected for recording. Pyramidal neurons were selected for recording based on their relative pyramidal shape and smooth, low-contrast appearance. To perform whole-cell patch clamp recordings, borosilicate glass pipettes (3–5 MΩ) were filled with intracellular solution (ICS) consisting of following (in mM): 110 K-gluconate, 10 KCl, 0.2 EGTA, 10 HEPES, 4 MgATP, 0.3 NaGTP, and 10 Na2-phosphocreatine (pH 7.3, 290–295 mOsmol/L) for current-clamp recordings and ICS containing of following (in mM) 120 CsCl, 5 NaCl, 1 MgCl2, 10 HEPES, 10 EGTA, 3 MgATP, 0.3 NaGTP (pH 7.3, 290–295 mOsmol/L) was used for sIPSC recordings. Data were collected using a Multiclamp 700B amplifier (Molecular Devices) and digitized at 10 kHz using Digidata 1550B and pClamp 11.1 software (Molecular Devices). The recordings were low pass filtered at 1 kHz. The access resistance was continuously monitored throughout the experiment, and data were included only if the holding current and series resistance remained stable (with less than a 25% change in the initial series resistance).

For the current-induced action potential analysis in interneurons, the resting membrane potential was recorded (in current-clamp mode) immediately after break-in and a series of 500 msec currents at increasing steps (–200 pA to +220 pA) were injected to neurons. Current-Clamp recordings were performed in aCSF. For sIPSC recording, 5 minutes after break-in, the recordings were initiated, and a total 2 minutes of recording was collected from each cell. IPSCs were pharmacologically isolated by adding blockers against the AMPA receptor (CNQX, 10 µM), NMDA receptor (APV, 50 µM) throughout the recordings. Data were extracted using threshold-based detection and analyzed for frequency and amplitude of events using Clampfit 11.1.

Transcriptomics

Bulk RNA Sequencing processing

Organoid tissue was processed for bulk RNA sequencing on day 50 and 100 of differentiation. 8-10 organoids were combined per sample, and RNA was extracted from 3 samples/patient line using the RNeasy mini kit and RNase-Free DNase set (Qiagen). RNA integrity was assessed with the 2100 Bioanalyzer to calculate the RNA integrity number (RIN), which we applied a cutoff of 8 before proceeding (Extended Data Fig. 3b). Library preparations were performed at TCAG (SickKids, Toronto, Canada) using the NEBNext Ultra II Direction RNA Library Prep kit from Illumina (New England Biolabs). mRNA was captured with purification beads and fragmented to 150 base pairs (bp) for cDNA synthesis. Stranded RNA was chosen for amplification given the increase in accuracy for transcript expression estimation[115]. The samples were run through a single lane on the Illumina NovaSeq 6000 S4 flow cell and a target capture of 30 million reads/sample was performed. Raw data was processed using the CutAdapt package to trim residual adapter content, and the STAR package (v2.7.11) using 2 Pass mode to align each read using the human GRCh38 reference genome. Quality control was performed using the FastQC platform, which enables high-throughput assessment of read quality using metrics such as read length, depth, Phred scores [116], and adapter contamination.

Bulk RNA Sequencing Analysis

Read integrity was assessed on raw RNA-seq data using FastQC (V0.11.5), followed by adapter trimming and filtering of low-quality reads via CutAdapt. Reads were mapped to hg38 using STAR (2-pass mode, V2.7.0A - outSAMtype BAM SortedByCoordinate) using default settings and the aligned read content was log2 normalized and assessed for differential gene expression (DGE) through the RStudio package, DESeq2 (V1.38.3). Briefly, low read counts (<10 reads in ≥50% of the samples) were removed to reduce technical noise and improve DEG detection sensitivity. Normalization and differential gene expression (DGE) analysis was performed using DESeq2. Covariate regression was used to regress batch effects, sex, and ancestry to minimize unnecessary variability in the dataset. Genes with an FDR <0.05 were deemed differentially expressed. Data was plotted using BioConductor and ggPlot2 packages in RStudio. Gene ontology (GO) term analysis was performed using ShinyGO (V0.8)[117] using default settings, and our filtered matrix gene set was used as a background to yield more accurate results. We selected enriched pathways within the range of 2-2 000 genes and FDR< 0.05 (based on the nominal p-value from the hypergeometric test). The default parameters used were 1 000 permutations, a minimal set size of 30, and a maximum set size of 500 to account for the large DEG datasets. Gene sets with FDR< 0.05 were considered significant.

Cell dissociation and processing for single cell RNA sequencing (scRNA Seq)

Neural organoids beyond 3 months of differentiation were cut first and washed 1x with PBS without Ca^{2+}/Mg^{2+} to remove potential necrotic tissue. All organoids were dissociated in live culture using a Papain dissociation kit (Worthington), using a modified protocol from Dr. Paola Arlotta's laboratory [118,119]. Cells with viability > 80% were resuspended in 0.01% BSA (diluted in 1x PBS) at a concentration of 1 200 cells/µL and shipped on ice for gel bead in emulsion (GEM) generation and downstream processing (SickKids). Cells used for fixed flexed assays were processed as per 10x Genomics Chromium Next GEM Single Cell Fixed RNA Sample Preparation Kit guidelines using a 24-hour PFA fixation protocol (10X Genomics, 1000414). Batch allocation was as follows: two batches of 15q13.3del families 1 and 3 forebrain organoids and three batches of 15q13.3del family 2 forebrain organoids were differentiated for the scRNA Seq experiment in Fig. 1.

Single cell RNA sequencing analysis

Raw FASTQ files were first aligned to the human genome GRCh38 using Cell Ranger's default alignment parameters 7.0.1 (10x Genomics). The Seurat R Package V.5.2.1 was then used for downstream processing[120]. First, low quality cells were removed through identification of high mitochondrial content (>15%) and abnormal read counts (<200 for poor read depth and >1 200 for doublets or multiplets)[120]. The matrix was then log-normalized, and regression was performed on the poor-quality cells and ancestral covariant as these are known contributors to variation[121]. Individual samples were aggregated into a single Seurat object, and the aggregate gene expression was scaled and normalized for each gene using a linear model that accounts for and normalizes by the sequence depth of each cell[120]. We used the FindVariableFeatures function to identify genes ("features") that are highly variable in the dataset, which were used to perform principal component analysis (PCA). The top 30 PCs were selected for clustering using Seurat's FindNeighbors function, followed by FindClusters with a resolution range of 0.4.

Cell variation was visualized by a Uniform Manifold Approximation and Projection (UMAP) plot and later annotated with cluster identities. Using a longitudinal unguided neural organoid (UNO) [122]and a human mid-gestation fetal cortex atlas as training material[98] as training data to identify the three most likely cell types within each predefined cluster. Frequency scores from scClassify were then used alongside manual annotations based on canonical cell type markers (Extended Data Fig. 3g). Reference datasets were imported as feature-barcode matrices or Seurat objects and preprocessed according to their source references. Frequency scores from scClassify were used to guide cell type annotation in combination with canonical marker expression. To focus on neural cell types and neurodevelopmental processes, mesenchymal-like cells, Choroid plexus (CP), and non-forebrain contaminant cell clusters labeled as 'unknown' (Unk) were excluded from downstream analysis.

Once cell populations were identified, DGE analysis was performed between genotypes for each cell type using the *FindMarkers* function, employing non-parametric Wilcoxon rank sum test with an adjusted p value based on the Bonferroni correction using all features in the dataset. Gene lists were filtered for FDR< 0.05 and an average log2fold change > log2(1.2) was applied for downstream gene ontology (GO) pathway analysis (g:Profiler2, V0.2.3). GO pathway analysis included enrichment terms for biological pathway, cellular compartment, and KEGG using ShinyGO (V0.8). Highly enriched genes were selected by filtering for DEGs with FDR < 0.0001 and a log2(0.8) < average log2FC > log2(1.2). DEG lists were screened for synaptic enrichment using the SynGO synaptic gene ontology enrichment analysis[60] tool (https://www.syngoportal.org) to obtain sunburst plots showing cellular compartment (CC) enrichment with second level terms displayed. We used the Monocle3 package (v1.4.26) for trajectory inference and pseudotime

analysis through Louvain clustering and assigned radial glia as the root node for downstream pseudotemporal ordering[57,123]. The resulting pseudotime distributions for all cells and each cell type between genotypes were compared using the *Kolmogorov-Smirnov* test. Module enrichment analysis was performed using Seurat's AddModuleScore function using default settings. ggplot2 was used for module score visualization, including percentile-based y-axis limits (1st–99th percentile) and coord_cartesian() to reduce the influence of extreme outliers visually. Statistical significance was assessed using a two-sided Wilcoxon rank-sum test with Benjamini–Hochberg adjustment.

Spatial RNA sequencing sample preparation (10x Genomics Visium HD)

Three hiPSC patient families (proband and familial control) were used to generate forebrain assembloids, of which a minimum of 3-5 replicates per line were used for the 10x Genomics Visium HD platform. Assembloids were processed using the 10x Genomics CytAssist Visium protocol for fixed frozen tissue. Briefly, samples were embedded in prechilled optimal cutting temperature (OCT) solution and submerged in isopentane over dry ice until frozen and stored at -80°C. 10 µm thick cryosections were adhered onto VWR SuperFrost Plus Slides, and following hematoxylin and eosin staining, sections were transferred onto the CytAssist Expression Slide Capture Area of the Visium Gene Expression slide. Samples were permeabilized and spot areas (8 µm) were captured for downstream reverse transcription and cDNA synthesis. Visium spatial gene expression libraries were then constructed and sequenced on the Illumina NovaSeq 6000 following sequencing recommendations. Duplicate sections were taken to assess RNA quality using the RNA Nano BioAnalyzer (Agilent). Only samples with a percentage of total RNA fragments > 200 nucleotides (DV200) scored to ≥70% and an RNA integrity number (RIN) > 4 were used for downstream sequencing and analysis (Extended Data Fig. 5a).

Spatial RNA sequencing data preprocessing and analysis

Spatial RNA sequencing reads were aligned using Space Ranger (10x Genomics) to the GRCh38 human reference genome. Spots not covering tissue were discarded manually in Loupe Browser (V8.0 10x Genomics) and additional filtering parameters (<10% mitochondrial content) were applied to ensure consistent sequencing quality throughout the tissue. Spatial data was then log-normalized and dimensionality reduction and clustering (Leiden) of the RNA expression data was performed using the Seurat V5 RStudio package. Spots were annotated using the scClassify function and inputting three training datasets, including our *in-house* day 100 forebrain organoid scRNA Seq (Fig. 1c, 10x Genomics fixed flex, down-sampled to one batch to reduce computational need) and the two datasets previously used for scRNA Seq annotation. The frequence scores were then used alongside manual annotations based on canonical cell type markers[124]. Region and cell type-specific differentially expressed genes (DEGs) were determined using the FindMarkers function using the Wilcoxon Rank Sum test with post-hoc test set to FDR (Extended Data Fig. 5d-e).

Gene Ontology (GO) enrichment analysis was performed on upregulated and downregulated genes separately for each cell type with the clusterProfiler (v.4.12.0) package, using the *org.Hs.eg.db* (v.3.20.0) database for human gene annotation. Enrichment was restricted to the Biological Process (BP) ontology, with significance defined as Benjamini–Hochberg (BH) adjusted *p*-value and *q*-value < 0.05. DNA Damage enrichment analysis was performed using the following filter terms: "*signal transduction in response to DNA damage*", "*positive regulation of DNA repair*", "[positive]/*regulation of DNA repair*", "[positive]/regulation of double-strand break repair", "double-strand break", "interstrand crosslink", "positive regulation of DNA break repair". Enrichment of selected terms was visualized through each cell type's respective gene counts and p values associated with each GO term.

Module enrichment analysis was performed using Seurat's AddModuleScore function using default settings. Gene sets were derived from significant (adjusted *p*-value and *q*-value < 0.05) GO terms from the following populations: Interneuron migration module (migratory MGE-InhibN, biological process), GABA-ergic synapse (migratory MGE-InhibN, biological process), Interstrand crosslink repair (ICR, total MGE-InhibNs, biological process), Signal transduction in response to DNA damage (migratory MGE-InhibN, biological process). Control *vs* 15q13.3del comparisons were performed separately within each subset (migrated and stationary) using Wilcoxon rank-sum tests, and p-values were adjusted for multiple testing with the Benjamini–Hochberg method.

Migration borders for spatially constrained DEG analysis (Visium HD) were constructed using the SPATA2 package[83] (3.1.0) using the getSpatAnnIds function and a combination of MGE lineage markers (*SST* and *NKX2-1*) in addition to the location of annotated cell types (Extended Data Fig. 5g). A migration border was defined as a region that had low NKX2-1 expression and sparse (> 5 adjacent spots) localized MGEhttps://bioinfogp.cnb.csic.es/tools/venny/. Slices lacking both dorsal and ventral markers—likely due to tilted sectioning that captured only one region—were excluded, as

they would not allow accurate quantification of migration across regions. Spatial annotations were added to the SPATA2 object and annotated spatial barcodes were used to subset each tissue domain[125125.]

Data and code availability

scRNA and spatial transcriptomics data from organoid tissue will be made available through GEO upon publication. Second trimester fetal cortex data is available from the CoDex viewer (http://solo.bmap.ucla.edu/shiny/webapp/). This paper does not report original code, however, primary software packages used for analysis are listed in the reporting summary. Any additional information required to reanalyze the data reported in this paper is available from the lead contact upon reasonable request.

Calcium imaging

Different viral labelling strategies were used for each calcium imaging experiment. For studying pan-inhibitory neuronal activity, dorsal-ventral assembloids of 5-month-old were infected with pAAV-mDlx-GCaMP6f-Fishell-2 (Addgene, 83899) at 1:100 dilution (Fig. 4a); for studying MGE neuronal activity, ventral organoids at d50 were infected with pAAV-mDlx-GCaMP6f-Fishell-2 (Addgene, 83899) at 1:500 dilution and fused with uninfected dorsal organoids (Fig. 4d); for measuring excitatory neuronal activity, dorsal organoids were infected with pENN.AAV.CamKII.GCaMP6f.WPRE.SV40 (Addgene, 100834) at 1: 500 dilution and fused with uninfected ventral organoids (Fig. 6a). In the latter two scenarios, fusion of organoids was made after 5 days of viral infection. Viral infection was performed in low-attachment 24-well plates containing 1 organoid/assembloid per well for 24 hours. They were maintained in forebrain maintenance media for one week followed by Brainphys media (STEMCELL Technologies, 08605) for 2-3 weeks. On the day of imaging, the infected organoids or assembloids were transferred to a 24-well glass bottom plate (Cellvis, P24-1.5H-N) containing Brainphys media and kept at 37 ℃, 5% CO_2. Imaging pan-inhibitory neuronal activity was performed using a confocal microscope with Airyscan (Zeiss, LSM 880) under 10 × objective with a field of view (FOVs) 425 µm x 425 µm at an acquisition rate of 5 frame per second. Imaging MGE and excitatory neuronal activity was performed using a Leica STELLARIS confocal microscope under 10 × objective at an image size of 582 µm x 582 µm and 7.55 frame per second. Spontaneous calcium activity was recorded for 5 minutes. 3 – 5 FOVs were recorded in every sample. Bath application of a calcium chelator BAPTA (Thermo Fisher Scientific, B1205) at 30 µM and of a voltage-gated sodium-channel antagonist TTX (Tocris, 1078) at 0.5 µM for 20 minutes was performed separately followed by recording of calcium activity for 5 minutes.

Calcium imaging analysis

The analysis of calcium imaging videos was carried out using Matlab as described previously[74]. ImageJ was first used to convert time-lapse images of each FOV per sample to binary images (tiff format), which were then processed by the Matlab script to produce a Maximum Intensity Projection (MIP). Within the MIP, active neurons were selected as regions of interest (ROI), and raw calcium traces were plotted by quantifying changes in fluorescence intensity within ROIs over the recording duration. To determine the network activity of each organoid/assembloid, the level of synchronicity of the active neurons within one FOV was measured and represented by the frequency and amplitude of synchronous peaks. By calculating the average intensity of all ROIs in one FOV for spike detection and deconvolution, synchronous peaks were identified based on a threshold determined by predefined percentile (mean + 1.5 standard deviation). Synchronized frequency was calculated as the number of detected synchronized peaks in one minute. Synchronized amplitude was calculated as the ratio of the increase in fluorescence (ΔF) normalized to the baseline (F_0), $\Delta F/F_0$, of the synchronized peaks. Single-neuron dynamics was defined as single-neuron frequency (the total number of detected peaks in one minute) and amplitude (the mean value of $\Delta F/F_0$ from all detected peaks) in individual calcium traces.

Monosynaptic Retrograde Viral Tracing

Monosynaptic retrograde viral tracing was achieved by using glycoprotein (G)-deleted rabies virus (RABV-EnvA-ΔG-GFP-F2, Neurophotonics Centre, University of Laval) and a helper AAV (AAV-CMV-TVA-mCherry-2A-oG or AAV-hDLx-TVA-mcherry-2A-oG, Neurophotonics Centre, University of Laval) that carries the G protein and TVA receptor which are required for transsynaptic retrograde labeling with the rabies virus. This is a two-part system where the first helper AAV infection delivers the EnVA receptor (TVA) and G protein into cells (“starter cells”), and only TVA-expressing starter cells can be infected by the second EnvA-pseudotyped, G-deleted rabies virus, producing live rabies virus coated with G protein which retrogradely crosses at synapses via G protein/G protein receptor signaling[126] and labels neurons forming synapses (presynaptic) onto the starter cells (postsynaptic)[69]. Once in the first order neurons, the G-deleted rabies virus cannot infect any subsequent neurons due to lack of G protein supply in the first order neurons, thus making it is mono-synaptically restricted[69]. Each assembloid was infected with the CMV helper AAV at 1:1000 dilution or the hDLx helper AAV at 1:500 dilution in low-attachment 24-well plates for 24 hours. After 3 weeks, the assembloids pre-infected with the helper AAV were infected with the rabies virus at the same viral dilution of the respective helper AAV overnight and were maintained for 1 more week. To show the rabies virus infection is dependent

on the helper AAV, a subset of assembloids were infected with the rabies virus only as a control experiment. The double-infected assembloids were then fixed in 4% PFA and cleared by the CUBIC method as described above. Whole-tissue light sheet imaging was performed under 4× objective in z-stack. The acquired images were analyzed using IMARIS 10.0, and spot analysis was used to quantify the number of mCherry positive cells, GFP positive cells representing pre-synaptic neurons, and GFP and mCherry double-positive cells representing starter cells/post-synaptic neurons that receive projection from GFP positive cells. A connectivity ratio between the number of GFP positive cells and the number of double-positive cells in the whole assembloid was calculated, as described previously[70].

COMET Assay

The neutral comet assay was performed using an adapted protocol from the Abcam comet assay kit (ab238544). Briefly, day 100 ventral organoid tissue was minced into small pieces using a sterile razor blade in 1 mL of ice-cold PBS containing 20 mM EDTA. This suspension was transferred to a 15 mL conical tube, where the supernatant was collected and centrifuged at 300 g for 7 minutes. Cells were resuspended at $1x10^6$ cells/mL in ice-cold PBS, which were then combined with melted comet agarose at 1/5 ratio (v/v). After triturating, 75 µl cell-agarose solution was immediately transferred onto the top of the comet agarose base layer on a 3-well slide. The cell-agarose solution was solidified at 4°C for 15 minutes followed by being transferred into lysis buffer for 60 minutes and finally transferred into alkaline solution for 30 minutes. All incubations were performed at 4°C using pre-chilled solutions. The slides were then placed inside an electrophoresis chamber filled with TBE solution, and an electric field of 3 volts/cm was applied for 15 minutes. Slides were washed 3x with chilled distilled water and 1x with chilled 70% ethanol for 5 minutes. Slides were air dried and then incubated with 100 µl per chamber of Vista Green DNA dye (1:10,000 dilution) for 15 minutes. Once dry, slides were imaged using a confocal microscope under a 10× objective lens.

Statistical Analysis

Statistical analyses of bulk and scRNA Seq data were performed by DESeq2, Seurat, CellChat, and Monocle3. Differential gene expression analysis was performed using the Wilcoxon rank sum test. All statistical analyses were performed on the R (version 4.4.0) software or GraphPad Prism (Version 8.0.0). For non-transcriptomic analyses in organoid experiments, a nested (hierarchical) mixed model was performed using the *lme4* (v1.1-35.1) and *lmerTest* (v3.1-3) R packages. Briefly, the normality of the data was assessed using Shapiro-Wilk test with $p > 0.05$ considered normal distribution – a linear mixed model was used for data analysis if the data were normal; a generalized linear mixed model was used if the data were not normal. In all the analyses, experimental conditions (e.g. genotypes) were determined as fixed effects (independent variables), and families of control and 15q13.3del were determined as random effects to account for variability between different families. Differences between more than 2 groups were analyzed using a one-way ANOVA with a post-hoc Tukey correction for multiple comparisons between every two groups. The only exception was when testing distributions, where we applied a Kolmogorov-Smirnov test instead. For statistical analysis in mouse experiments, GraphPad Prism (Version 8.0.0) was used, and Shapiro-Wilk test was used for normality test followed by an unpaired two-tailed Student's t-test for normally distributed datasets or a Mann-Whitney-U test for non-normally distributed datasets. p-values below 0.05 were considered statistically significant in this research. All error bars represent mean ± S.E.M. unless otherwise stated.

References

[1] S. Kilpatrick, C. Irwin, and K.K. Singh, "Human pluripotent stem cell (hPSC) and organoid models of autism: opportunities and limitations," Transl Psychiatry **13**(1), 217 (2023).

[2] F. Birey, M.Y. Li, A. Gordon, M. V. Thete, A.M. Valencia, O. Revah, A.M. Paşca, D.H. Geschwind, and S.P. Paşca, "Dissecting the molecular basis of human interneuron migration in forebrain assembloids from Timothy syndrome," Cell Stem Cell **29**(2), (2022).

[3] T.A. Khan, O. Revah, A. Gordon, S.-J. Yoon, A.K. Krawisz, C. Goold, Y. Sun, C.H. Kim, Y. Tian, M.-Y. Li, J.M. Schaepe, K. Ikeda, N.D. Amin, N. Sakai, M. Yazawa, L. Kushan, S. Nishino, M.H. Porteus, J.L. Rapoport, J.A. Bernstein, R. O'Hara, C.E. Bearden, J.F. Hallmayer, J.R. Huguenard, D.H. Geschwind, R.E. Dolmetsch, and S.P. Paşca, "Neuronal defects in a human cellular model of 22q11.2 deletion syndrome," Nat Med **26**(12), 1888–1898 (2020).

[4] A. de Thonel, J.K. Ahlskog, K. Daupin, V. Dubreuil, J. Berthelet, C. Chaput, G. Pires, C. Leonetti, R. Abane, L.C. Barris, I. Leray, A.L. Aalto, S. Naceri, M. Cordonnier, C. Benasolo, M. Sanial, A. Duchateau, A. Vihervaara, M.C. Puustinen, F. Miozzo, P. Fergelot, É. Lebigot, A. Verloes, P. Gressens, D. Lacombe, J. Gobbo, C. Garrido, S.D. Westerheide, L. David, M. Petitjean, O. Taboureau, F. Rodrigues-Lima, S. Passemard, D. Sabéran-Djoneidi, L. Nguyen, M. Lancaster, L. Sistonen, and V. Mezger, "CBP-HSF2 structural and functional interplay in Rubinstein-Taybi neurodevelopmental disorder," Nat Commun **13**(1), 7002 (2022).

[5] J. Urresti, P. Zhang, P. Moran-Losada, N.-K. Yu, P.D. Negraes, C.A. Trujillo, D. Antaki, M. Amar, K. Chau, A.B. Pramod, J. Diedrich, L. Tejwani, S. Romero, J. Sebat, J.R. Yates III, A.R. Muotri, and L.M. Iakoucheva, "Correction: Cortical organoids model early brain development disrupted by 16p11.2 copy number variants in autism," Mol Psychiatry **26**(12), 7581–7581 (2021).

[6] R. Sebastian, K. Jin, N. Pavon, R. Bansal, A. Potter, Y. Song, J. Babu, R. Gabriel, Y. Sun, B. Aronow, and C.H. Pak, "Schizophrenia-associated NRXN1 deletions induce developmental-timing- and cell-type-specific vulnerabilities in human brain organoids," Nat Commun **14**(1), (2023).

[7] A. Jourdon, F. Wu, J. Mariani, D. Capauto, S. Norton, L. Tomasini, A. Amiri, M. Suvakov, J.D. Schreiner, Y. Jang, A. Panda, C.K. Nguyen, E.M. Cummings, G. Han, K. Powell, A. Szekely, J.C. McPartland, K. Pelphrey, K. Chawarska, P. Ventola, A. Abyzov, and F.M. Vaccarino, "Modeling idiopathic autism in forebrain organoids reveals an imbalance of excitatory cortical neuron subtypes during early neurogenesis," Nat Neurosci **26**(9), 1505–1515 (2023).

[8] C. Li, J.S. Fleck, C. Martins-Costa, T.R. Burkard, J. Themann, M. Stuempflen, A.M. Peer, Á. Vertesy, J.B. Littleboy, C. Esk, U. Elling, G. Kasprian, N.S. Corsini, B. Treutlein, and J.A. Knoblich, "Single-cell brain organoid screening identifies developmental defects in autism," Nature **621**(7978), 373–380 (2023).

[9] F. Birey, J. Andersen, C.D. Makinson, S. Islam, W. Wei, N. Huber, H.C. Fan, K.R.C. Metzler, G. Panagiotakos, N. Thom, N.A. O'Rourke, L.M. Steinmetz, J.A. Bernstein, J. Hallmayer, J.R. Huguenard, and S.P. Pasca, "Assembly of functionally integrated human forebrain spheroids," Nature **545**(7652), 54–59 (2017).

[10] M.M. Onesto, J. Kim, and S.P. Pasca, "Assembloid models of cell-cell interaction to study tissue and disease biology," Cell Stem Cell, (2024).

[11] J. Andersen, O. Revah, Y. Miura, N. Thom, N.D. Amin, K.W. Kelley, M. Singh, X. Chen, M.V. Thete, E.M. Walczak, H. Vogel, H.C. Fan, and S.P. Paşca, "Generation of Functional Human 3D Cortico-Motor Assembloids," Cell **183**(7), 1913-1929.e26 (2020).

[12] F. Birey, and S.P. Paşca, "Imaging neuronal migration and network activity in human forebrain assembloids," STAR Protoc **3**(3), (2022).

[13] J.-I. Kim, Y. Miura, M.-Y. Li, O. Revah, S. Selvaraj, F. Birey, X. Meng, M.V. Thete, S.D. Pavlov, J. Andersen, A.M. Paşca, M.H. Porteus, J.R. Huguenard, and S.P. Paşca, "Human assembloids reveal the consequences of CACNA1G gene variants in the thalamocortical pathway," (2023).

[14] X. Meng, D. Yao, X. Chen, K.W. Kelley, N. Reis, M.V. Thete, S. Kulkarni, M.C. Bassik, and S.P. Paşca, "CRISPR screens in 3D assembloids reveal disease genes associated with human interneuron development," 2022 (n.d.).

[15] Y. Miura, M.Y. Li, F. Birey, K. Ikeda, O. Revah, M.V. Thete, J.Y. Park, A. Puno, S.H. Lee, M.H. Porteus, and S.P. Paşca, "Generation of human striatal organoids and cortico-striatal assembloids from human pluripotent stem cells," Nat Biotechnol **38**(12), 1421–1430 (2020).

[16] J.A. Bagley, D. Reumann, S. Bian, J. Lévi-Strauss, and J.A. Knoblich, "Fused cerebral organoids model interactions between brain regions," Nat Methods **14**(7), 743–751 (2017).

[17] D. Reumann, C. Krauditsch, M. Novatchkova, E. Sozzi, S.N. Wong, M. Zabolocki, M. Prioure, B. Doleschall, K.I. Ritzau-Reid, M. Piber, I. Morassut, C. Fieseler, A. Fiorenzano, M.M. Stevens, M. Zimmer, C. Bardy, M. Parmar, and J.A. Knoblich, "In vitro modeling of the human dopaminergic system using spatially arranged ventral midbrain–striatum–cortex assembloids," Nat Methods **20**(12), 2034–2047 (2023).

[18] C. Bosone, D. Castaldi, T.R. Burkard, S.J. Guzman, T. Wyatt, C. Cheroni, N. Caporale, S. Bajaj, J.A. Bagley, C. Li, B. Sorre, C.E. Villa, G. Testa, V. Krenn, and J.A. Knoblich, "A polarized FGF8 source specifies frontotemporal signatures in spatially oriented cell populations of cortical assembloids," Nat Methods **21**(11), 2147–2159 (2024).

[19] Y. Xiang, Y. Tanaka, B. Patterson, Y.-J. Kang, G. Govindaiah, N. Roselaar, B. Cakir, K.-Y. Kim, A.P. Lombroso, S.-M. Hwang, M. Zhong, E.G. Stanley, A.G. Elefanty, J.R. Naegele, S.-H. Lee, S.M. Weissman, and I.-H. Park, "Fusion of Regionally Specified hPSC-Derived Organoids Models Human Brain Development and Interneuron Migration," Cell Stem Cell **21**(3), 383-398.e7 (2017).

[20] A.S. Bassett, E.W.C. Chow, J. Husted, R. Weksberg, O. Caluseriu, G.D. Webb, and M.A. Gatzoulis, "Clinical features of 78 adults with 22q11 deletion syndrome," Am J Med Genet A **138A**(4), 307–313 (2005).
[21] L. Willatt, J. Cox, J. Barber, E.D. Cabanas, A. Collins, D. Donnai, D.R. FitzPatrick, E. Maher, H. Martin, J. Parnau, L. Pindar, J. Ramsay, C. Shaw-Smith, E.A. Sistermans, M. Tettenborn, D. Trump, B.B.A. de Vries, K. Walker, and F.L. Raymond, "3q29 Microdeletion Syndrome: Clinical and Molecular Characterization of a New Syndrome," The American Journal of Human Genetics **77**(1), 154–160 (2005).
[22] M. Richter, N. Murtaza, R. Scharrenberg, S.H. White, O. Johanns, S. Walker, R.K.C. Yuen, B. Schwanke, B. Bedürftig, M. Henis, S. Scharf, V. Kraus, R. Dörk, J. Hellmann, Z. Lindenmaier, J. Ellegood, H. Hartung, V. Kwan, J. Sedlacik, J. Fiehler, M. Schweizer, J.P. Lerch, I.L. Hanganu-Opatz, F. Morellini, S.W. Scherer, K.K. Singh, and F. Calderon de Anda, "Altered TAOK2 activity causes autism-related neurodevelopmental and cognitive abnormalities through RhoA signaling," Mol Psychiatry, 1 (2018).
[23] M. Niarchou, S.J.R.A. Chawner, J.L. Doherty, A.M. Maillard, S. Jacquemont, W.K. Chung, L. Green-Snyder, R.A. Bernier, R.P. Goin-Kochel, E. Hanson, D.E.J. Linden, S.C. Linden, F.L. Raymond, D. Skuse, J. Hall, M.J. Owen, and M.B.M. van den Bree, "Psychiatric disorders in children with 16p11.2 deletion and duplication," Transl Psychiatry **9**(1), 8 (2019).
[24] S.C. Linden, C.J. Watson, J. Smith, S.J.R.A. Chawner, T.M. Lancaster, F. Evans, N. Williams, D. Skuse, F.L. Raymond, J. Hall, M.J. Owen, D.E.J. Linden, L. Green-Snyder, W.K. Chung, A.M. Maillard, S. Jacquemont, and M.B.M. van den Bree, "The psychiatric phenotypes of 1q21 distal deletion and duplication," Transl Psychiatry **11**(1), 105 (2021).
[25] I. Helbig, H.C. Mefford, A.J. Sharp, M. Guipponi, M. Fichera, A. Franke, H. Muhle, C. De Kovel, C. Baker, S. Von Spiczak, K.L. Kron, I. Steinich, A.A. Kleefuß-Lie, C. Leu, V. Gaus, B. Schmitz, K.M. Klein, P.S. Reif, F. Rosenow, Y. Weber, H. Lerche, F. Zimprich, L. Urak, K. Fuchs, M. Feucht, P. Genton, P. Thomas, F. Visscher, G.J. De Haan, R.S. Møller, H. Hjalgrim, D. Luciano, M. Wittig, M. Nothnagel, C.E. Elger, P. Nürnberg, C. Romano, A. Malafosse, B.P.C. Koeleman, D. Lindhout, U. Stephani, S. Schreiber, E.E. Eichler, and T. Sander, "15q13.3 microdeletions increase risk of idiopathic generalized epilepsy," Nat Genet **41**(2), 160–162 (2009).
[26] A.J. Sharp, H.C. Mefford, K. Li, C. Baker, C. Skinner, R.E. Stevenson, R.J. Schroer, F. Novara, M. De Gregori, R. Ciccone, A. Broomer, I. Casuga, Y. Wang, C. Xiao, C. Barbacioru, G. Gimelli, B.D. Bernardina, C. Torniero, R. Giorda, R. Regan, V. Murday, S. Mansour, M. Fichera, L. Castiglia, P. Failla, M. Ventura, Z. Jiang, G.M. Cooper, S.J.L. Knight, C. Romano, O. Zuffardi, C. Chen, C.E. Schwartz, and E.E. Eichler, "A recurrent 15q13.3 microdeletion syndrome associated with mental retardation and seizures," Nat Genet **40**(3), 322–328 (2008).
[27] M. Shinawi, C.P. Schaaf, S.S. Bhatt, Z. Xia, A. Patel, S.W. Cheung, B. Lanpher, S. Nagl, H.S. Herding, C. Nevinny-Stickel, L.L. Immken, G.S. Patel, J.R. German, A.L. Beaudet, and P. Stankiewicz, "A small recurrent deletion within 15q13.3 is associated with a range of neurodevelopmental phenotypes," Nat Genet **41**(12), 1269–1271 (2009).
[28] C. Lowther, G. Costain, D.J. Stavropoulos, R. Melvin, C.K. Silversides, D.M. Andrade, J. So, H. Faghfoury, A.C. Lionel, C.R. Marshall, S.W. Scherer, and A.S. Bassett, "Delineating the 15q13.3 microdeletion phenotype: A case series and comprehensive review of the literature," Genetics in Medicine **17**(2), 149–157 (2015).
[29] L.M. Dibbens, S. Mullen, I. Helbig, H.C. Mefford, M.A. Bayly, S. Bellows, C. Leu, H. Trucks, T. Obermeier, M. Wittig, A. Franke, H. Caglayan, Z. Yapici, T. Sander, E.E. Eichler, I.E. Scheffer, J.C. Mulley, S.F. Berkovic, P. De Jonghe, A. Suls, H. Hjalgrim, J.M. Madsen, R.S. Møller, A.E. Lehesjoki, A. Siren, V. Gaus, D. Janz, B. Schmitz, C.E. Elger, K. Hallmann, A.A. Kleefuß-Lie, W.S. Kunz, A. Raabe, H. Muhle, P. Ostertag, S. von Spiczak, U. Stephani, H. Lerche, Y.G. Weber, P. Striano, F. Zara, C. Marini, E.H. Brilstra, D. Kastelijn-Nolst Trenité, B.P.C. Koeleman, C.G.F. de Kovel, D. Lindhout, M.E.M. Swinkels, D. Yalcin, B. Baykan, D. Turkdogan, G. Dizdarer, C. Ozkara, Y. Lee, J. Müller-Quernheim, R. Fölster-Holst, S. Hofmann, A. Nebel, S. Schreiber, M. Schürmann, E. Rodriguez, S. Weidinger, H. Baurecht, B.A. Lie, K.M. Boberg, and T.H. Karlsen, "Familial and sporadic 15q13.3 microdeletions in idiopathic generalized epilepsy: Precedent for disorders with complex inheritance," Hum Mol Genet **18**(19), 3626–3631 (2009).
[30] B.K. Unda, L. Chalil, S. Yoon, S. Kilpatrick, C. Irwin, S. Xing, N. Murtaza, A. Cheng, C. Brown, A. Afonso, E. McCready, G.M. Ronen, J. Howe, A. Caye-Eude, A. Verloes, B.W. Doble, L. Faivre, A. Vitobello, S.W. Scherer, Y. Lu, P. Penzes, and K.K. Singh, "Impaired OTUD7A-dependent Ankyrin regulation mediates neuronal dysfunction in mouse and human models of the 15q13.3 microdeletion syndrome," Mol Psychiatry **28**(4), 1747–1769 (2023).
[31] M. Uddin, B.K. Unda, V. Kwan, N.T. Holzapfel, S.H. White, L. Chalil, M. Woodbury-Smith, K.S. Ho, E. Harward, N. Murtaza, B. Dave, G. Pellecchia, L. D'Abate, T. Nalpathamkalam, S. Lamoureux, J. Wei, M. Speevak, J. Stavropoulos, K.J. Hope, B.W. Doble, J. Nielsen, E.R. Wassman, S.W. Scherer, and K.K. Singh, "OTUD7A Regulates Neurodevelopmental Phenotypes in the 15q13.3 Microdeletion Syndrome," The American Journal of Human Genetics **102**(2), 278–295 (2018).
[32] S. Zhang, X. Zhang, C. Purmann, S. Ma, A. Shrestha, K.N. Davis, M. Ho, Y. Huang, R. Pattni, W.H. Wong, J.A. Bernstein, J. Hallmayer, and A.E. Urban, "Network Effects of the 15q13.3 Microdeletion on the Transcriptome and Epigenome in Human-Induced Neurons," Biol Psychiatry **89**(5), 497–509 (2021).
[33] J. Thelin, P. Halje, J. Nielsen, M. Didriksen, P. Petersson, and J.F. Bastlund, "The translationally relevant mouse model of the 15q13.3 microdeletion syndrome reveals deficits in neuronal spike firing matching clinical neurophysiological biomarkers seen in schizophrenia," Acta Physiologica **220**(1), 124–136 (2017).
[34] A. Jourdon, S. Scuderi, D. Capauto, A. Abyzov, and F.M. Vaccarino, "PsychENCODE and beyond: transcriptomics and epigenomics of brain development and organoids," Neuropsychopharmacology **46**(1), 70–85 (2021).
[35] L. Rylaarsdam, J. Rakotomamonjy, E. Pope, and A. Guemez-Gamboa, "iPSC-derived models of PACS1 syndrome reveal transcriptional and functional deficits in neuron activity," Nat Commun **15**(1), 827 (2024).

[36] M. Pigoni, A. Uzquiano, B. Paulsen, A.J. Kedaigle, S.M. Yang, P. Symvoulidis, X. Adiconis, S. Velasco, R. Sartore, K. Kim, A. Tucewicz, S.Y. Tropp, K. Tsafou, X. Jin, L. Barrett, F. Chen, E.S. Boyden, A. Regev, J.Z. Levin, and P. Arlotta, "Cell-type specific defects in *PTEN* -mutant cortical organoids converge on abnormal circuit activity," Hum Mol Genet **32**(18), 2773–2786 (2023).
[37] R.H. Purcell, E. Sefik, E. Werner, A.T. King, T.J. Mosley, M.E. Merritt-Garza, P. Chopra, Z.T. McEachin, S. Karne, N. Raj, B.J. Vaglio, D. Sullivan, B.L. Firestein, K. Tilahun, M.I. Robinette, S.T. Warren, Z. Wen, V. Faundez, S.A. Sloan, G.J. Bassell, and J.G. Mulle, "Cross-species analysis identifies mitochondrial dysregulation as a functional consequence of the schizophrenia-associated 3q29 deletion," Sci Adv **9**(33), (2023).
[38] Y. Perez, D. Velmeshev, L. Wang, M.L. White, C. Siebert, J. Baltazar, G. Zuo, J.A. Moriano, S. Chen, D.M. Steffen, N.G. Dutton, S. Wang, B. Wick, M. Haeussler, S. Chamberlain, A. Alvarez-Buylla, and A. Kriegstein, "Single-cell analysis of dup15q syndrome reveals developmental and postnatal molecular changes in autism," Nature Communications **16**(1), (2025).
[39] L. Lim, D. Mi, A. Llorca, and O. Marín, "Development and Functional Diversification of Cortical Interneurons," Neuron **100**(2), 294–313 (2018).
[40] *On GABAergic Interneuron Diversity and Maturation* (n.d.).
[41] L. Wang, C. Wang, J.A. Moriano, S. Chen, G. Zuo, A. Cebrián-Silla, S. Zhang, T. Mukhtar, S. Wang, M. Song, L.G. de Oliveira, Q. Bi, J.J. Augustin, X. Ge, M.F. Paredes, E.J. Huang, A. Alvarez-Buylla, X. Duan, J. Li, and A.R. Kriegstein, "Molecular and cellular dynamics of the developing human neocortex at single-cell resolution," (2024).
[42] L. Garma, K. Institutet, L. Harder, J. Barba-Reyes, M. Diez-Salguero, A. Serrano-Pozo, B. Hyman, and A. Munoz-Manchado, "Interneuron diversity in the human dorsal striatum," (2023).
[43] Y. Yu, Z. Zeng, D. Xie, R. Chen, Y. Sha, S. Huang, W. Cai, W. Chen, W. Li, R. Ke, and T. Sun, "Interneuron origin and molecular diversity in the human fetal brain," Nat Neurosci **24**(12), 1745–1756 (2021).
[44] J. Mariani, G. Coppola, P. Zhang, A. Abyzov, L. Provini, L. Tomasini, M. Amenduni, A. Szekely, D. Palejev, M. Wilson, M. Gerstein, E.L. Grigorenko, K. Chawarska, K.A. Pelphrey, J.R. Howe, and F.M. Vaccarino, "FOXG1-Dependent Dysregulation of GABA/Glutamate Neuron Differentiation in Autism Spectrum Disorders.," Cell **162**(2), 375–390 (2015).
[45] B. Paulsen, S. Velasco, A.J. Kedaigle, M. Pigoni, G. Quadrato, A.J. Deo, X. Adiconis, A. Uzquiano, R. Sartore, S.M. Yang, S.K. Simmons, P. Symvoulidis, K. Kim, K. Tsafou, A. Podury, C. Abbate, A. Tucewicz, S.N. Smith, A. Albanese, L. Barrett, N.E. Sanjana, X. Shi, K. Chung, K. Lage, E.S. Boyden, A. Regev, J.Z. Levin, and P. Arlotta, "Autism genes converge on asynchronous development of shared neuron classes.," Nature **602**(7896), 268–273 (2022).
[46] F. Pipicelli, N. Baumann, R. Di Giaimo, A. Forero-Echeverry, C. Kyrousi, R. Bonrath, G. Maccarrone, D. Jabaudon, and S. Cappello, "Non-cell-autonomous regulation of interneuron specification mediated by extracellular vesicles.," Sci Adv **9**(20), eadd8164 (2023).
[47] F. Di Matteo, F. Pipicelli, C. Kyrousi, I. Tovecci, E. Penna, M. Crispino, A. Chambery, R. Russo, A.C. Ayo-Martin, M. Giordano, A. Hoffmann, E. Ciusani, L. Canafoglia, M. Götz, R. Di Giaimo, and S. Cappello, "Cystatin B is essential for proliferation and interneuron migration in individuals with EPM1 epilepsy.," EMBO Mol Med **12**(6), e11419 (2020).
[48] R.M. Walsh, G.W. Crabtree, K. Kalpana, L. Jubierre, S.Y. Koo, G. Ciceri, J.A. Gogos, I. Kruglikov, and L. Studer, "Forebrain assembloids support the development of fast-spiking human PVALB+ cortical interneurons and uncover schizophrenia-associated defects," Neuron, (2025).
[49] S. Velasco, A.J. Kedaigle, S.K. Simmons, A. Nash, M. Rocha, G. Quadrato, B. Paulsen, L. Nguyen, X. Adiconis, A. Regev, J.Z. Levin, and P. Arlotta, "Individual brain organoids reproducibly form cell diversity of the human cerebral cortex," Nature **570**(7762), 523–527 (2019).
[50] N. Hoppman-Chaney, K. Wain, P. Seger, D. Superneau, and J. Hodge, "Identification of single gene deletions at 15q13.3: further evidence that *CHRNA7* causes the 15q13.3 microdeletion syndrome phenotype," Clin Genet **83**(4), 345–351 (2013).
[51] J. Yin, W. Chen, E.S. Chao, S. Soriano, L. Wang, W. Wang, S.E. Cummock, H. Tao, K. Pang, Z. Liu, F.A. Pereira, R.C. Samaco, H.Y. Zoghbi, M. Xue, and C.P. Schaaf, "Otud7a Knockout Mice Recapitulate Many Neurological Features of 15q13.3 Microdeletion Syndrome," The American Journal of Human Genetics **102**(2), 296–308 (2018).
[52] N. Gass, W. Weber-Fahr, A. Sartorius, R. Becker, M. Didriksen, T.B. Stensbøl, J.F. Bastlund, A. Meyer-Lindenberg, and A.J. Schwarz, "An acetylcholine alpha7 positive allosteric modulator rescues a schizophrenia-associated brain endophenotype in the 15q13.3 microdeletion, encompassing CHRNA7.," Eur Neuropsychopharmacol **26**(7), 1150–60 (2016).
[53] A. Kozlova, S. Zhang, A. V. Kotlar, B. Jamison, H. Zhang, S. Shi, M.P. Forrest, J. McDaid, D.J. Cutler, M.P. Epstein, M.E. Zwick, Z.P. Pang, A.R. Sanders, S.T. Warren, P. V. Gejman, J.G. Mulle, and J. Duan, "Loss of function of OTUD7A in the schizophrenia- associated 15q13.3 deletion impairs synapse development and function in human neurons," The American Journal of Human Genetics **109**(8), 1500–1519 (2022).
[54] J.B. LePichon, D.C. Bittel, W.D. Graf, and S. Yu, "A 15q13.3 homozygous microdeletion associated with a severe neurodevelopmental disorder suggests putative functions of the TRPM1, CHRNA7, and other homozygously deleted genes," Am J Med Genet A **152**(5), 1300–1304 (2010).
[55] M.A. Gillentine, J. Yin, A. Bajic, P. Zhang, S. Cummock, J.J. Kim, and C.P. Schaaf, "Functional Consequences of CHRNA7 Copy-Number Alterations in Induced Pluripotent Stem Cells and Neural Progenitor Cells," The American Journal of Human Genetics **101**(6), 874–887 (2017).

[56] T.J. Nowakowski, A. Bhaduri, A.A. Pollen, B. Alvarado, M.A. Mostajo-Radji, E. Di Lullo, M. Haeussler, C. Sandoval-Espinosa, S.J. Liu, D. Velmeshev, J.R. Ounadjela, J. Shuga, X. Wang, D.A. Lim, J.A. West, A.A. Leyrat, W.J. Kent, and A.R. Kriegstein, "Spatiotemporal gene expression trajectories reveal developmental hierarchies of the human cortex," Science (1979) **358**(6368), 1318–1323 (2017).
[57] J. Cao, M. Spielmann, X. Qiu, X. Huang, D.M. Ibrahim, A.J. Hill, F. Zhang, S. Mundlos, L. Christiansen, F.J. Steemers, C. Trapnell, and J. Shendure, "The single-cell transcriptional landscape of mammalian organogenesis," Nature **566**(7745), 496–502 (2019).
[58] Z. Mo, A.R. Moore, R. Filipovic, Y. Ogawa, I. Kazuhiro, S.D. Antic, and N. Zecevic, "Human Cortical Neurons Originate from Radial Glia and Neuron-Restricted Progenitors," The Journal of Neuroscience **27**(15), 4132–4145 (2007).
[59] U.C. Eze, A. Bhaduri, M. Haeussler, T.J. Nowakowski, and A.R. Kriegstein, "Single-cell atlas of early human brain development highlights heterogeneity of human neuroepithelial cells and early radial glia," Nat Neurosci **24**(4), 584–594 (2021).
[60] F. Koopmans, P. van Nierop, M. Andres-Alonso, A. Byrnes, T. Cijsouw, M.P. Coba, L.N. Cornelisse, R.J. Farrell, H.L. Goldschmidt, D.P. Howrigan, N.K. Hussain, C. Imig, A.P.H. de Jong, H. Jung, M. Kohansalnodehi, B. Kramarz, N. Lipstein, R.C. Lovering, H. MacGillavry, V. Mariano, H. Mi, M. Ninov, D. Osumi-Sutherland, R. Pielot, K.H. Smalla, H. Tang, K. Tashman, R.F.G. Toonen, C. Verpelli, R. Reig-Viader, K. Watanabe, J. van Weering, T. Achsel, G. Ashrafi, N. Asi, T.C. Brown, P. De Camilli, M. Feuermann, R.E. Foulger, P. Gaudet, A. Joglekar, A. Kanellopoulos, R. Malenka, R.A. Nicoll, C. Pulido, J. de Juan-Sanz, M. Sheng, T.C. Südhof, H.U. Tilgner, C. Bagni, À. Bayés, T. Biederer, N. Brose, J.J.E. Chua, D.C. Dieterich, E.D. Gundelfinger, C. Hoogenraad, R.L. Huganir, R. Jahn, P.S. Kaeser, E. Kim, M.R. Kreutz, P.S. McPherson, B.M. Neale, V. O'Connor, D. Posthuma, T.A. Ryan, C. Sala, G. Feng, S.E. Hyman, P.D. Thomas, A.B. Smit, and M. Verhage, "SynGO: An Evidence-Based, Expert-Curated Knowledge Base for the Synapse," Neuron **103**(2), 217-234.e4 (2019).
[61] S.P. Paşca, P. Arlotta, H.S. Bateup, J.G. Camp, S. Cappello, F.H. Gage, J.A. Knoblich, A.R. Kriegstein, M.A. Lancaster, G.-L. Ming, A.R. Muotri, I.-H. Park, O. Reiner, H. Song, L. Studer, S. Temple, G. Testa, B. Treutlein, and F.M. Vaccarino, "A nomenclature consensus for nervous system organoids and assembloids," Nature **609**(7929), 907–910 (2022).
[62] N. Murtaza, A.A. Cheng, C.O. Brown, D.P. Meka, S. Hong, J.A. Uy, J. El-Hajjar, N. Pipko, B.K. Unda, B. Schwanke, S. Xing, B. Thiruvahindrapuram, W. Engchuan, B. Trost, E. Deneault, F. Calderon de Anda, B.W. Doble, J. Ellis, E. Anagnostou, G.D. Bader, S.W. Scherer, Y. Lu, and K.K. Singh, "Neuron-specific protein network mapping of autism risk genes identifies shared biological mechanisms and disease-relevant pathologies," Cell Rep **41**(8), (2022).
[63] S.J.B. Butt, M. Fuccillo, S. Nery, S. Noctor, A. Kriegstein, J.G. Corbin, and G. Fishell, "The Temporal and Spatial Origins of Cortical Interneurons Predict Their Physiological Subtype," Neuron **48**(4), 591–604 (2005).
[64] G. Quattrocolo, G. Fishell, and T.J. Petros, "Heterotopic Transplantations Reveal Environmental Influences on Interneuron Diversity and Maturation," Cell Rep **21**(3), 721–731 (2017).
[65] A. Mukhopadhyay, T. McGuire, C.-Y. Peng, and J.A. Kessler, "Differential effects of BMP signaling on parvalbumin and somatostatin interneuron differentiation," Development **136**(15), 2633–2642 (2009).
[66] N. V. De Marco García, T. Karayannis, and G. Fishell, "Neuronal activity is required for the development of specific cortical interneuron subtypes," Nature **472**(7343), 351–355 (2011).
[67] R. Priya, M.F. Paredes, T. Karayannis, N. Yusuf, X. Liu, X. Jaglin, I. Graef, A. Alvarez-Buylla, and G. Fishell, "Activity Regulates Cell Death within Cortical Interneurons through a Calcineurin-Dependent Mechanism," Cell Rep **22**(7), 1695–1709 (2018).
[68] G. Pouchelon, D. Dwivedi, Y. Bollmann, C.K. Agba, Q. Xu, A.M.C. Mirow, S. Kim, Y. Qiu, E. Sevier, K.D. Ritola, R. Cossart, and G. Fishell, "The organization and development of cortical interneuron presynaptic circuits are area specific," Cell Rep **37**(6), 109993 (2021).
[69] I.R. Wickersham, D.C. Lyon, R.J.O. Barnard, T. Mori, S. Finke, K.-K. Conzelmann, J.A.T. Young, and E.M. Callaway, "Monosynaptic Restriction of Transsynaptic Tracing from Single, Genetically Targeted Neurons," Neuron **53**(5), 639–647 (2007).
[70] S. Falkner, S. Grade, L. Dimou, K.K. Conzelmann, T. Bonhoeffer, M. Götz, and M. Hübener, "Transplanted embryonic neurons integrate into adult neocortical circuits," Nature **539**(7628), 248–253 (2016).
[71] S.R. Fair, D. Julian, A.M. Hartlaub, S.T. Pusuluri, G. Malik, T.L. Summerfied, G. Zhao, A.B. Hester, W.E. Ackerman, E.W. Hollingsworth, M. Ali, C.A. McElroy, I.A. Buhimschi, J. Imitola, N.L. Maitre, T.A. Bedrosian, and M.E. Hester, "Electrophysiological Maturation of Cerebral Organoids Correlates with Dynamic Morphological and Cellular Development," Stem Cell Reports **15**(4), 855–868 (2020).
[72] T.K. Matsui, M. Matsubayashi, Y.M. Sakaguchi, R.K. Hayashi, C. Zheng, K. Sugie, M. Hasegawa, T. Nakagawa, and E. Mori, "Six-month cultured cerebral organoids from human ES cells contain matured neural cells," Neurosci Lett **670**, 75–82 (2018).
[73] L.O. Porciúncula, L. Goto-Silva, P.F. Ledur, and S.K. Rehen, "The Age of Brain Organoids: Tailoring Cell Identity and Functionality for Normal Brain Development and Disease Modeling," Front Neurosci **15**, (2021).
[74] Z. Sun, and T.C. Südhof, "A simple Ca2+-imaging approach to neural network analyses in cultured neurons," J Neurosci Methods **349**, (2021).
[75] K. Fejgin, J. Nielsen, M.R. Birknow, J.F. Bastlund, V. Nielsen, J.B. Lauridsen, H. Stefansson, S. Steinberg, H.B.D. Sorensen, T.E. Mortensen, P.H. Larsen, I. V. Klewe, S. V. Rasmussen, K. Stefansson, T.M. Werge, P. Kallunki, K. V. Christensen, and M. Didriksen, "A mouse model that recapitulates cardinal features of the 15q13.3 microdeletion syndrome including schizophrenia- and epilepsy-related alterations," Biol Psychiatry, (2014).

[76] B. Rudy, G. Fishell, S. Lee, and J. Hjerling-Leffler, "Three groups of interneurons account for nearly 100% of neocortical GABAergic neurons," Dev Neurobiol **71**(1), 45–61 (2011).
[77] X. Xu, K.D. Roby, and E.M. Callaway, "Immunochemical characterization of inhibitory mouse cortical neurons: Three chemically distinct classes of inhibitory cells," Journal of Comparative Neurology **518**(3), 389–404 (2010).
[78] A.-R. Al-Absi, P. Qvist, S. Glerup, C. Sanchez, and J.R. Nyengaard, "Df(h15q13)/+ Mouse Model Reveals Loss of Astrocytes and Synaptic-Related Changes of the Excitatory and Inhibitory Circuits in the Medial Prefrontal Cortex," Cerebral Cortex **31**(3), 1609–1621 (2021).
[79] S. Malwade, J. Gasthaus, C. Bellardita, M. Andelic, B. Moric, I. Korshunova, O. Kiehn, N.A. Vasistha, and K. Khodosevich, "Identification of Vulnerable Interneuron Subtypes in 15q13.3 Microdeletion Syndrome Using Single-Cell Transcriptomics," Biol Psychiatry **91**(8), 727–739 (2022).
[80] V. Singhal, N. Chou, J. Lee, Y. Yue, J. Liu, W.K. Chock, L. Lin, Y.-C. Chang, E.M.L. Teo, J. Aow, H.K. Lee, K.H. Chen, and S. Prabhakar, "BANKSY unifies cell typing and tissue domain segmentation for scalable spatial omics data analysis," Nat Genet **56**(3), 431–441 (2024).
[81] A. Barile, I. Nogués, M.L. di Salvo, V. Bunik, R. Contestabile, and A. Tramonti, "Molecular characterization of pyridoxine 5'-phosphate oxidase and its pathogenic forms associated with neonatal epileptic encephalopathy," Sci Rep **10**(1), 13621 (2020).
[82] L. Larsson, L. Franzé, P.L. Stå Hl, and J. Lundeberg, "Gene expression," (n.d.).
[83] J. Kueckelhaus, S. Frerich, J. Kada-Benotmane, C. Koupourtidou, J. Ninkovic, M. Dichgans, J. Beck, O. Schnell, and D.H. Heiland, "Inferring histology-associated gene expression gradients in spatial transcriptomic studies," Nat Commun **15**(1), 7280 (2024).
[84] Y. Nakamura, S.-I. Sakakibara, T. Miyata, M. Ogawa, T. Shimazaki, S. Weiss, R. Kageyama, and H. Okano, *The BHLH Gene Hes1 as a Repressor of the Neuronal Commitment of CNS Stem Cells* (1999).
[85] A.A.S.F. Raposo, F.F. Vasconcelos, D. Drechsel, C. Marie, C. Johnston, D. Dolle, A. Bithell, S. Gillotin, D.L.C. van den Berg, L. Ettwiller, P. Flicek, G.E. Crawford, C.M. Parras, B. Berninger, N.J. Buckley, F. Guillemot, and D.S. Castro, "Ascl1 coordinately regulates gene expression and the chromatin landscape during neurogenesis," Cell Rep **10**(9), 1544–1556 (2015).
[86] Y.H. Liu, J.W. Tsai, J.L. Chen, W.S. Yang, P.C. Chang, P.L. Cheng, D.L. Turner, Y. Yanagawa, T.W. Wang, and J.Y. Yu, "Ascl1 promotes tangential migration and confines migratory routes by induction of Ephb2 in the telencephalon," Sci Rep **7**, (2017).
[87] B. McAllister, J. Donaldson, C.S. Binda, S. Powell, U. Chughtai, G. Edwards, J. Stone, S. Lobanov, L. Elliston, L.N. Schuhmacher, E. Rees, G. Menzies, M. Ciosi, A. Maxwell, M.J. Chao, E.P. Hong, D. Lucente, V. Wheeler, J.M. Lee, M.E. MacDonald, J.D. Long, E.H. Aylward, G.B. Landwehrmeyer, A.E. Rosser, J.S. Paulsen, N.M. Williams, J.F. Gusella, D.G. Monckton, N.D. Allen, P. Holmans, L. Jones, and T.H. Massey, "Exome sequencing of individuals with Huntington's disease implicates FAN1 nuclease activity in slowing CAG expansion and disease onset," Nat Neurosci **25**(4), 446–457 (2022).
[88] R. Goold, M. Flower, D.H. Moss, C. Medway, A. Wood-Kaczmar, R. Andre, P. Farshim, G.P. Bates, P. Holmans, L. Jones, and S.J. Tabrizi, "FAN1 modifies Huntington's disease progression by stabilizing the expanded *HTT* CAG repeat," Hum Mol Genet **28**(4), 650–661 (2019).
[89] H. Wood, "FAN1 nuclease helps to delay Huntington disease," Nat Rev Neurol **18**(6), 317–317 (2022).
[90] I. Ionita-Laza, B. Xu, V. Makarov, J.D. Buxbaum, J.L. Roos, J.A. Gogos, and M. Karayiorgou, "Scan statistic-based analysis of exome sequencing data identifies FAN1 at 15q13.3 as a susceptibility gene for schizophrenia and autism," Proc Natl Acad Sci U S A **111**(1), 343–348 (2014).
[91] R. Wang, N.S. Persky, B. Yoo, O. Ouerfelli, A. Smogorzewska, S.J. Elledge, and N.P. Pavletich, "Mechanism of DNA interstrand cross-link processing by repair nuclease FAN1," Science (1979) **346**(6213), 1127–1130 (2014).
[92] A. Smogorzewska, R. Desetty, T.T. Saito, M. Schlabach, F.P. Lach, M.E. Sowa, A.B. Clark, T.A. Kunkel, J.W. Harper, M.P. Colaiácovo, and S.J. Elledge, "A Genetic Screen Identifies FAN1, a Fanconi Anemia-Associated Nuclease Necessary for DNA Interstrand Cross-link Repair," Mol Cell **39**(1), 36–47 (2010).
[93] V.N. Shah, B. Chagot, and W.J. Chazin, "Calcium-Dependent Regulation of Ion Channels.," Calcium Bind Proteins **1**(4), 203–212 (2006).
[94] P. Alcamí, and A.E. Pereda, "Beyond plasticity: the dynamic impact of electrical synapses on neural circuits," Nat Rev Neurosci **20**(5), 253–271 (2019).
[95] N. Caporale, D. Castaldi, M.T. Rigoli, C. Cheroni, S. Trattaro, A. Valenti, M. Bonfanti, S. Stucchi, A.L. Tobon, D. Ricca, M. Lessi, M. Pezzali, A. Vitriolo, K.T. Schmid, M. Heinig, F.J. Theis, C.E. Villa, and G. Testa, "Multiplexing cortical brain organoids for the longitudinal dissection of developmental traits at single cell resolution," (2023).
[96] D.J.C. Tai, P. Razaz, S. Erdin, D. Gao, J. Wang, X. Nuttle, C.E. de Esch, R.L. Collins, B.B. Currall, K. O'Keefe, N.D. Burt, R. Yadav, L. Wang, K. Mohajeri, T. Aneichyk, A. Ragavendran, A. Stortchevoi, E. Morini, W. Ma, D. Lucente, A. Hastie, R.J. Kelleher, R.H. Perlis, M.E. Talkowski, and J.F. Gusella, "Tissue- and cell-type-specific molecular and functional signatures of 16p11.2 reciprocal genomic disorder across mouse brain and human neuronal models," The American Journal of Human Genetics **109**(10), 1789–1813 (2022).
[97] G. Lavallée, G. Andelfinger, M. Nadeau, C. Lefebvre, G. Nemer, M.E. Horb, and M. Nemer, "The Kruppel-like transcription factor KLF13 is a novel regulator of heart development," EMBO J **25**(21), 5201–5213 (2006).
[98] D. Polioudakis, L. de la Torre-Ubieta, J. Langerman, A.G. Elkins, X. Shi, J.L. Stein, C.K. Vuong, S. Nichterwitz, M. Gevorgian, C.K. Opland, D. Lu, W. Connell, E.K. Ruzzo, J.K. Lowe, T. Hadzic, F.I. Hinz, S. Sabri, W.E. Lowry, M.B. Gerstein, K. Plath, and D.H.

Geschwind, “A Single-Cell Transcriptomic Atlas of Human Neocortical Development during Mid-gestation,” Neuron **103**(5), 785-801.e8 (2019).
[99] A. Asenjo-Martinez, K. Dragicevic, W.-H. Hou, A. Ozsvar, N. Winther Hansen, U. Pfisterer, R. Rydbirk, S. Demharter, B.E. Møller, J. Gasthaus, I. Korshunova, J.-F. Perrier, M. Capogna, N.A. Vasistha, and K. Khodosevich, “Dysfunction of cortical GABAergic projection neurons as a major hallmark in a model of neuropsychiatric syndrome,” Neuron, (2025).
[100] T.D. Prévôt, F. Gastambide, C. Viollet, N. Henkous, G. Martel, J. Epelbaum, D. Béracochéa, and J.-L. Guillou, “Roles of Hippocampal Somatostatin Receptor Subtypes in Stress Response and Emotionality,” Neuropsychopharmacology **42**(8), 1647–1656 (2017).
[101] C.E. Page, R. Shepard, K. Heslin, and L. Coutellier, “Prefrontal parvalbumin cells are sensitive to stress and mediate anxiety-related behaviors in female mice,” Sci Rep **9**(1), 19772 (2019).
[102] D. Kvitsiani, S. Ranade, B. Hangya, H. Taniguchi, J.Z. Huang, and A. Kepecs, “Distinct behavioural and network correlates of two interneuron types in prefrontal cortex,” Nature **498**(7454), 363–366 (2013).
[103] J. Wang, Y. Kong, X. Li, Y. Tan, K. Xiang, J.C. Izpisua Belmonte, and L. Shi, “DNA replication fork speed Acts as an Engine in Cortical Neurogenesis,” (2024).
[104] E.-L. Yap, and M.E. Greenberg, “Activity-Regulated Transcription: Bridging the Gap between Neural Activity and Behavior,” Neuron **100**(2), 330–348 (2018).
[105] R. Madabhushi, F. Gao, A.R. Pfenning, L. Pan, S. Yamakawa, J. Seo, R. Rueda, T.X. Phan, H. Yamakawa, P.-C. Pao, R.T. Stott, E. Gjoneska, A. Nott, S. Cho, M. Kellis, and L.-H. Tsai, “Activity-Induced DNA Breaks Govern the Expression of Neuronal Early-Response Genes,” Cell **161**(7), 1592–1605 (2015).
[106] X.N. Zhao, and K. Usdin, “FAN1 protects against repeat expansions in a Fragile X mouse model,” DNA Repair (Amst) **69**, 1–5 (2018).
[107] M. Ishahak, R.H. Han, D. Annamalai, T. Woodiwiss, C. McCornack, R.T. Cleary, P.A. DeSouza, X. Qu, S. Dahiya, A.H. Kim, and J.R. Millman, “Modeling glioblastoma tumor progression via CRISPR-engineered brain organoids,” (2024).
[108] P.P. Hsu, A.S. Conchola, T. Frum, X. Dong, L. Tudrick, V. Ponnusamy, M.S. Downey, M. Wu, M. Yang, Y. Lee, E. Niestroy, Y.-H. Tsai, A. Wu, I.A. Glass, S.D. Merajver, and J.R. Spence, “A spatially-resolved blueprint of the developing human lung reveals a WNT-driven niche for basal stem cells,” (2024).
[109] H. Quach, S. Farrell, M.J.M. Wu, K. Kanagarajah, J.W.-H. Leung, X. Xu, P. Kallurkar, A.L. Turinsky, C.E. Bear, F. Ratjen, B. Kalish, S. Goyal, T.J. Moraes, and A.P. Wong, “Early human fetal lung atlas reveals the temporal dynamics of epithelial cell plasticity,” Nat Commun **15**(1), 5898 (2024).
[110] S. Deguchi, K. Kosugi, N. Takeishi, Y. Watanabe, S. Morimoto, R. Negoro, F. Yokoi, H. Futatsusako, M. Nakajima-Koyama, M. Iwasaki, T. Yamamoto, Y. Kawaguchi, Y. Torisawa, and K. Takayama, “Construction of multilayered small intestine-like tissue by reproducing interstitial flow,” Cell Stem Cell **31**(9), 1315-1326.e8 (2024).
[111] S.L. Giandomenico, M. Sutcliffe, and M.A. Lancaster, “Generation and long-term culture of advanced cerebral organoids for studying later stages of neural development,” Nat Protoc **16**(2), 579–602 (2021).
[112] Y. Shi, L. Sun, M. Wang, J. Liu, S. Zhong, R. Li, P. Li, L. Guo, A. Fang, R. Chen, W.-P. Ge, Q. Wu, and X. Wang, “Vascularized human cortical organoids (vOrganoids) model cortical development in vivo,” PLoS Biol **18**(5), e3000705 (2020).
[113] B. Cakir, Y. Xiang, Y. Tanaka, M.H. Kural, M. Parent, Y.-J. Kang, K. Chapeton, B. Patterson, Y. Yuan, C.-S. He, M.S.B. Raredon, J. Dengelegi, K.-Y. Kim, P. Sun, M. Zhong, S. Lee, P. Patra, F. Hyder, L.E. Niklason, S.-H. Lee, Y.-S. Yoon, and I.-H. Park, “Engineering of human brain organoids with a functional vascular-like system,” Nat Methods **16**(11), 1169–1175 (2019).
[114] S. Nojima, E.A. Susaki, K. Yoshida, H. Takemoto, N. Tsujimura, S. Iijima, K. Takachi, Y. Nakahara, S. Tahara, K. Ohshima, M. Kurashige, Y. Hori, N. Wada, J.I. Ikeda, A. Kumanogoh, E. Morii, and H.R. Ueda, “CUBIC pathology: Three-dimensional imaging for pathological diagnosis,” Sci Rep **7**(1), (2017).
[115] S. Zhao, Y. Zhang, W. Gordon, J. Quan, H. Xi, S. Du, D. von Schack, and B. Zhang, “Comparison of stranded and non-stranded RNA-seq transcriptome profiling and investigation of gene overlap,” BMC Genomics **16**(1), (2015).
[116] M.D. MacManes, “On the optimal trimming of high-throughput mRNA sequence data,” Front Genet **5**(JAN), (2014).
[117] S. Xijin Ge, D. Jung, and R. Yao, “ShinyGO: a graphical gene-set enrichment tool for animals and plants,” (n.d.).
[118] S. Velasco, B. Paulsen, and P. Arlotta, “Highly reproducible human brain organoids recapitulate cerebral cortex cellular diversity,” (2019).
[119] J. Sherwood, G. Quadrato^*^, J.L. Sherwood^*^, and P. Arlotta, “Long-term culture and electrophysiological characterization of human brain organoids,” Protoc Exch, (2017).
[120] R. Satija, J.A. Farrell, D. Gennert, A.F. Schier, and A. Regev, “Spatial reconstruction of single-cell gene expression data,” Nat Biotechnol **33**(5), (2015).
[121] G. Chen, B. Ning, and T. Shi, “Single-cell RNA-seq technologies and related computational data analysis,” Front Genet **10**(APR), (2019).
[122] S. Kanton, M.J. Boyle, Z. He, M. Santel, A. Weigert, F. Sanchís-Calleja, P. Guijarro, L. Sidow, J.S. Fleck, D. Han, Z. Qian, M. Heide, W.B. Huttner, P. Khaitovich, S. Pääbo, B. Treutlein, and J.G. Camp, “Organoid single-cell genomic atlas uncovers human-specific features of brain development,” Nature **574**(7778), (2019).

[123] C. Trapnell, D. Cacchiarelli, J. Grimsby, P. Pokharel, S. Li, M. Morse, N.J. Lennon, K.J. Livak, T.S. Mikkelsen, and J.L. Rinn, "The dynamics and regulators of cell fate decisions are revealed by pseudotemporal ordering of single cells," Nat Biotechnol **32**(4), 381–386 (2014).

[124] S. Sona, M. Bradley, and A.H. Ting, "Protocols for single-cell RNA-seq and spatial gene expression integration and interactive visualization," STAR Protoc **4**(1), (2023).

[125] S. Jin, C.F. Guerrero-Juarez, L. Zhang, I. Chang, R. Ramos, C.H. Kuan, P. Myung, M. V. Plikus, and Q. Nie, "Inference and analysis of cell-cell communication using CellChat," Nat Commun **12**(1), (2021).

[126] R. Etessami, K.-K. Conzelmann, B. Fadai-Ghotbi, B. Natelson, H. Tsiang, and P.-E. Ceccaldi, "Spread and pathogenic characteristics of a G-deficient rabies virus recombinant: an in vitro and in vivo study," Journal of General Virology **81**(9), 2147–2153 (2000).

[127] K. Kratz, B. Schöpf, S. Kaden, A. Sendoel, R. Eberhard, C. Lademann, E. Cannavó, A. A. Sartori, M. O. Hengartner, and J. Jiricny, "Deficiency of FANCD2-associated nuclease KIAA1018/FAN1 sensitizes cells to interstrand crosslinking agents," Cell 142(1), 77–88 (2010). doi: 10.1016/j.cell.2010.06.022.

[128] C. MacKay, A.–C. Déclais, C. Lundin, A. Agostinho, A. J. Deans, T. J. MacArtney, K. Hofmann, A. Gartner, S. C. West, T. Helleday, D. M. J. Lilley, and J. Rouse, "Identification of KIAA1018/FAN1, a DNA repair nuclease recruited to DNA damage by monoubiquitinated FANCD2," Cell 142(1), 65–76 (2010). doi: 10.1016/j.cell.2010.06.021.

[129] J. Kim, K. Imaizumi, O. Jurjuț, K. W. Kelley, D. Wang, M. V. Thete, Z. Hudacova, N. Reis, M. Kaganovsky, O. Onesto, N. Sakai, J. Hao. X. Meng, S. Nishino, J. Huguenard, S. Pașca, "Human assembloid model of the ascending neural sensory pathway," Nature 642(8066), 143–153 (2025). PMCID: PMC12137141.

[130] B. Huang, Z. Zeng, S. Kim, C. C. Fausto, K. Koppitch, H. Li, Z. Li, X. Chen, J. Guo, C. C. Zhang, T. Ma, P. Medina, M. E. Schreiber, M. W. Xia, A. C. Vonk, T. Xiang, T. Patel, Y. Li, R. K. Parvez, B. Der, J. H. Chen, Z. Liu, M. E. Thornton, B. H. Grubbs, Y. Diao, Y. Dou, K. Gnedeva, Q. Ying, N. M. Pastor-Soler, T. Fei, K. R. Hallows, N. O. Lindström, A. P. McMahon, Z. Li, "Spatially patterned kidney assembloids recapitulate progenitor self-assembly and enable high-fidelity in vivo disease modeling," Cell Stem Cell 32(10), 1614–1633.e13 (2025).

[131] Y. Miura, J. I. Kim, O. Jurjuț, K. W. Kelley, D. Wang, M. V. Thete, Z. Hudacova, N. Reis, M. Kaganovsky, O. Onesto, N. Sakai, J. Hao, X. Meng, S. Nishino, J. Huguenard, S. Pașca, "Assembloid model to study loop circuits of the human nervous system," preprint at bioRxiv (2024). doi: 10.1101/2024.10.13.617729.

[132] J. Li, A. Wiesinger, L. Fokkert, P. Bakker, D. K. de Vries, A. J. Tijsen, Y. M. Pinto, A. O. Verkerk, V. M. Christoffels, G. J. J. Boink, and H. D. Devalla, "Modeling the atrioventricular conduction axis using human pluripotent stem cell-derived cardiac assembloids," Cell Stem Cell 32(9), 1359–1375.e7 (2024). doi: 10.1016/j.stem.2024.08.008; PMCID: PMC11546832.

Acknowledgements

We thank members of the Singh, Bains and Hope labs for reading the manuscript. The study was supported by the Canadian Institutes of Health Research (CIHR), the Ontario Brain Institute (OBI), the National Science and Engineering Research Council (NSERC) of Canada, the Donald K. Johnson Eye Institute (DKJEI), and the Krembil Research Institute (KRI), the Brain & Behavior Research Foundation (BBRF).

Author contributions

This study was designed by KKS and SK. The majority of the experiments were performed by SK, with assistance from LN, XER, ZD, JU, AC, YP, and HTC. SK developed and analyzed the transcriptomic experimental pipelines, assembloid migration assays, iPSC reprogramming and editing, organoid culturing, and immunofluorescence assays. LN performed all rabies monosynaptic tracing experiments and CamkII-calcium imaging. XER completed Dlx-calcium imaging and DNA damage immunofluorescence experiments. ZD performed patch clamp electrophysiology experiments. AC reprogrammed Family 4-6 iPSCs. YP grew forebrain organoids for biochemical assays. scRNA seq analyses were modified from a script written by JU. Bulk RNA Seq preprocessing was assisted by HTC. MEP and NC engineered rabies virus for monosynaptic tracing experiments. JH performed patient recruitment, consent and sample collection. Data were analyzed and figures were prepared by SK and LN. SK, LN and KKS wrote the manuscript.

Declaration of interests

SK is employed by Genentech. Other authors declare no conflict of interest.

Materials & Correspondence

Correspondences and material requests should be made to Dr. Karun Singh, karun.singh@uhn.ca

Supplemental information

Extended Data Figures: Extended Data Fig. 1-5.
Supplementary Table 1: 15q13.3del forebrain bulk RNA Seq DEGs related to Fig. 1b.
Supplementary Table 2: scRNA Seq DEG list for all forebrain organoid cell types related to Fig. 1.
Supplementary Table 3: Spatial Seq DEG list for all forebrain assembloid cell types related to Fig. 3.
Supplementary Table 4: Spatial RNA Seq GO term enrichment of upregulated DEGs in migrated MGE-InhibNs related to Fig. 3.
Supplementary Table 5: Spatial RNA Seq GO term enrichment of all forebrain assembloid cell types related to Fig. 3.

Supplementary Video 1: Pre-BAPTA treatment of pAAV-mDlx-GCaMP6f-Fishell-2-infected assembloids.
Supplementary Video 2: Post-BAPTA treatment of pAAV-mDlx-GCaMP6f-Fishell-2-infected assembloids.
Supplementary Video 3: Pre-TTX treatment of pAAV-mDlx-GCaMP6f-Fishell-2-infected assembloids.
Supplementary Video 4: Post-TTX treatment of pAAV-mDlx-GCaMP6f-Fishell-2-infected assembloids.

Supplementary Files

This is a list of supplementary files associated with this preprint. Click to download.

- SupplementaryTable2.xlsx
- ExtendedDataFigures.pdf
- SupplementaryTable4.xlsx
- SupplementaryTable5.xlsx
- SupplementaryVideo4.avi
- SupplementaryTable3.xlsx
- SupplementaryVideo3.avi
- SupplementaryTable1.xlsx
- SupplementaryVideo2.avi
- SupplementaryVideo1.avi